
Flux density measurements of TeV blazars with the Effelsberg 100 m telescope

Author:
Jonas Heßdörfer

Supervisor:
Prof. Dr. Matthias Kadler



*A thesis submitted in fulfillment of the requirements
for the degree of Bachelor of Science*

in the group of

Prof. Dr. Matthias Kadler
Chair of Astronomy

Abstract

Active galactic nuclei (AGN) lie in the center of active galaxies and are one of the most luminous and most powerful non-explosive phenomena in the Universe, oftentimes outshining their entire host galaxy by several orders of magnitude. The current unification scheme of AGN describes them as a super-massive black hole accreting matter onto an accretion disk and different classes arise as an effect of orientation. Sources for which the ratio of radio to optical emission is considerably larger than unity are called radio-loud and feature collimated jets of plasma. When the angle to the line-of-sight of the jet axis is small, these sources are called blazars and appear even brighter than regular AGN due to Doppler boosting. They show a characteristic dumbbell-hump structure when plotting their spectral energy distribution (SED). Blazars are subdivided into BL Lacs and flat spectrum radio quasars (FSRQ), but the main interest of this work lies on so-called high-peaked BL Lac objects (HBL) that have their primary emission peak above frequencies $\nu \sim 10^{15}$ Hz. As Donato et al. (2001) showed, fainter blazars accelerate particles to higher energies than brighter blazars do. Extreme blazars can reach even higher energies, as was shown by Biteau et al. (2020). Therefore, HBLs are generally very weak radio sources.

Determining the Doppler factor of the jets of these TeV emitting blazars results in two different, incompatible values, depending on whether they were calculated through the variability timescale or via very-long baseline interferometry measurements of the apparent jet speed (Piner & Edwards, 2015). This was termed the Doppler crisis and has yet to be solved.

For this thesis, a total of 38 sources were considered, including 25 HBLs, with 11 of them being extreme blazars. Although similar studies were already done by the likes of Lindfors et al. (2016), Angelakis et al. (2019) and Piner & Edwards (2018), this work, together with further observations and analyses of the sample, will lay the basics for the first statistical comparison of extreme blazars and other TeV-emitting AGN. The sample contains well known sources such as Mrk 421, TXS 0506+056 and BL Lacertae, but also sources such as 4FGL J0658.6+0636 that only recently became interesting.

All observations were conducted with the Effelsberg 100 m radio telescope. As one of the biggest fully steerable single-dish radio telescopes worldwide, it has a high angular resolution and a high sensitivity, making it possible to detect the faint radio signals from HBLs.

For the observations, two secondary focus receivers centered around wavelengths of $\lambda = 1.3$ cm and $\lambda = 7$ mm were used, each again splitting into four frequency bands. The telescope does so-called cross-scans, where it slues over the position of the source in two perpendicular directions. It measures the antenna temperature, or rather the system temperature, which will then step-by-step be corrected and turned into a flux density with the unit Jansky. Before this happens, each scan has to go through a quality check and will potentially be edited to improve the fit to the data. Subtracting the signal of a second horn helps to further improve the scan by removing weather effects. The scans are then successively corrected for pointing offsets, atmospheric effects and gain elevation losses. Final flux density values are derived by comparing the measured flux densities of observed calibration sources with their expected ones. Multiple scans for a single source are averaged using their weighted mean.

Data considered in this work were taken from several observational sessions spread over a couple of months, with the main focus being the epoch of the 21.09.2020. Reducing the data of every source reveals that most of them have flux densities in the range of 0.1 Jy to 1 Jy, with a few bright and faint exceptions. On the contrary, HBLs are mostly weaker than 0.4 Jy and are overall the weakest sources in the sample. The spectral index α of each source is determined by plotting its flux densities against the corresponding frequency on a logarithmic scale and using a linear fit. A Kolmogorov-Smirnov test was run to see if the spectral indices of the HBLs follow a normal distribution centered around $\alpha = 0$. On a 2.9σ significance level, this can be ruled out, suggesting that HBLs are not typical blazars.

Aktive Galaxienkerne (AGN) gehören zu den leuchtkräftigsten und stärksten nicht explosiven Objekten im ganzen Universum. Sie liegen im Inneren von aktiven Galaxien und können die Leuchtkraft ihrer Heimatgalaxie um mehrere Größenordnungen übertreffen. Die vereinigende Theorie der AGN beschreibt sie als supermassereiche schwarze Löcher, die umgebende Materie auf eine Akkretionsscheibe akkretieren. Verschiedene Klassifizierungen der AGN entstehen dabei aus ihrer relativen Orientierung bezüglich eines Beobachters. Radio-laute AGN weisen eine deutlich höhere Leuchtkraft im Radiobereich als im optischen Bereich auf und zeigen zweiseitige Jets aus kollimiertem Plasma. Ist der Winkel zwischen der Achse des Jets und der Sichtlinie klein, so bezeichnet man den AGN als Blazar; diese erscheinen aufgrund von relativistischem Beaming heller als andere AGN. Ihre spektrale Energiedichte zeigt eine charakteristische Doppelhöckerstruktur. Die Klasse der Blazare kann noch weiter in die Unterklassen der BL Lac Objekte und der flat spectrum radio quasars (FSRQ) geteilt werden. Dabei liegt der Fokus dieser Arbeit auf den BL Lacs, deren primäre Emission über einer Frequenz von $\nu \sim 10^{15}$ Hz liegt und deshalb high-peaked BL Lac Objekte (HBL) genannt werden. [Donato et al. \(2001\)](#) zeigten, dass schwächere Blazare Teilchen zu höheren Energien beschleunigen als leuchtkräftigere Blazare, und [Biteau et al. \(2020\)](#) stellten fest, dass die Maxima der Emission von sogenannten extremen Blazaren um zwei Größenordnungen nach oben verschoben sein können. HBLs sind daher generell sehr schwache Radioquellen.

Werden die Dopplerfaktoren der Jets von HBLs bestimmt, so hängt das Ergebnis von der Methode ab. Variabilitätsargumente liefern sehr hohe Dopplerfaktoren, während die Bestimmung der scheinbaren Jetgeschwindigkeiten durch very-long baseline interferometry moderate Dopplerfaktoren ergibt. Diese Diskrepanz wird weitläufig als Dopplerkrise bezeichnet und wurde noch nicht endgültig gelöst.

In dieser Arbeit wurden insgesamt 38 Quellen betrachtet, wobei 25 davon HBLs sind und davon wiederum 11 als extreme Blazare gelten. Ähnliche Studien wurden unter anderem von [Lindfors et al. \(2016\)](#), [Angelakis et al. \(2019\)](#) und [Piner & Edwards \(2018\)](#) durchgeführt, jedoch wird durch diese und folgende Arbeiten zum ersten Mal ein statistischer Vergleich zwischen extremen Blazaren und anderen TeV-emittierenden Quellen möglich sein. Der Quellkatalog enthält dabei einige bekannte Quellen wie Mrk 421, TXS 0506+056 und BL Lacertae, aber auch einige erst kürzlich interessant gewordene Quellen wie 4FGL J0658.6+0636.

Die Beobachtungen der Quellen wurden dabei mit dem 100 m Radioteleskop in Effelsberg durchgeführt. Mit der großen Schüssel erreicht es ein hohes Auflösungsvermögen sowie eine hohe Sensitivität, womit selbst die schwachen HBLs detektiert werden können.

Verwendet wurden dafür zwei Receiver, die jeweils bei Wellenlängen um $\lambda = 1.3$ cm und $\lambda = 7$ mm messen, die sich noch weiter in vier Frequenzbänder aufteilen. Das Teleskop bewegt sich dabei in zwei zueinander senkrechten Richtungen über die Quelle und misst die Antennen- beziehungsweise die Systemtemperatur. Um diese Temperatur in die gängig verwendete Größe Jansky für die Flussdichte einer Quelle umzuwandeln sind mehrere Schritte und Korrekturen nötig. Die Qualität einzelner Scans wird überprüft und diese potentiell bearbeitet, um einen besseren Gaußfit an das Signal zu ermöglichen. Das Abziehen eines zweiten Signals kann dabei Wettereffekte minimieren. Danach werden weitere Korrekturen durchgeführt, die fehlerhafte Ausrichtungen des Teleskops, Dämpfung des Signals durch die Atmosphäre und Fehler durch den elevationsbedingten Verlust des Antennengewinns ausgleichen sollen. Finale Flussdichtewerte der Quellen entstehen durch Vergleich von beobachteten Kalibrationsquellen mit deren erwarteten Flussdichten und gewichtetem Mittelwert einzelner Scans.

Für diese Arbeit wurden die Quellen über mehrere Monate hinweg beobachtet, die meisten Daten kommen aber von der Beobachtungsepoche vom 21.09.2020. Die Auswertung zeigt, dass die meisten Quellen, bis auf wenige Ausnahmen, eine Flussdichte im Bereich von 0.1 Jy bis 1 Jy aufweisen. HBLs sind dabei größtenteils schwächer als 0.4 Jy und bilden die insgesamt schwächste Gruppe der betrachteten Quellen. Die Spektralindizes α der Quellen wurden durch Auftragung der Flussdichten gegen die zugehörigen Frequenzen in einem doppel-logarithmischen Plot und einem anschließenden linearen Fit bestimmt. Ein Kolmogorov-Smirnov Test auf Normalverteilung der Spektralindizes der HBL um $\alpha = 0$ wurde durchgeführt. Dieser ergab auf einem 2.9σ Signifikanzniveau, dass die Werte keiner Standardnormalverteilung folgen, was für die Besonderheit der HBL spricht.

Contents

Abstract	3
Zusammenfassung	5
1 TeV blazars in the radio regime	9
1.1 Active galactic nuclei	9
1.2 The blazar sequence	11
1.3 High-peaked BL Lacs	13
1.4 Doppler crisis	13
2 Introducing the sample	17
3 Observations and data reduction	21
3.1 The Effelsberg 100m telescope	21
3.2 Observing with the Effelsberg telescope	23
3.3 Data reduction of pointed flux measurements	26
4 Results	33
5 Conclusion and outlook	37
Bibliography	39
Acknowledgments	41
Declaration of authorship	42
Appendices	43
Appendix A Spectra and data table	45
Appendix B A guide to reducing pointed flux measurements obtained by the Effelsberg 100 m telescope	57

1 | TeV blazars in the radio regime

Electromagnetic radiation of different wavelengths (or frequencies) build up the electromagnetic spectrum. The long wavelength (low frequency) part of the spectrum is called the radio regime. It roughly ranges from 3 kHz (~ 100 km) up to 900 GHz (~ 0.3 mm). While this boundary is somewhat arbitrary and can vary between different conventions, regardless, radio waves make up the low energy part of the spectrum.

Sources of astrophysical radio waves are manifold, ranging from the Sun, over the cosmic microwave background, to entire galaxies. The radio sources of interest for this work are so-called active galactic nuclei (AGN).

1.1 Active galactic nuclei

While the luminosity of most galaxies is dominated by thermal emission from the stars in the galaxy, the cores of active galaxies, called AGN, can outshine their host galaxy by many orders of magnitude. Reaching bolometric luminosities up to $L_{\text{bol}} \approx 10^{48}$ erg/s, they are the most powerful non-explosive sources known in the Universe¹ (Padovani et al., 2017). Contrary to normal galaxies, which peak at optical wavelengths, AGN emit radiation over the entire electromagnetic spectrum, producing much more long and short wavelength emission. Additionally, their flux and polarization can change within minutes, as shown by Albert et al. (2007). Based on source coherence arguments, the size of the continuum-emitting region can be inferred to be of order of light days (or $\lesssim 0.1$ pc), as a source can only vary coherently if the entire region is causally connected. The emission region, therefore, is contained well within the innermost part of the galaxy, the nucleus, justifying the name.

Producing such high luminosities in a very compact region of space cannot be ascribed to nuclear fusion like in stars, but is now rather attributed to an accreting super-massive black hole (SMBH) in the center of an AGN. This is the foundation of the currently accepted unification scheme of AGN, as described by Antonucci (1993) and Urry & Padovani (1995). For historical reasons, there are many different names for different types of AGN, as they were classified according to their measured properties when they were first discovered. However, there are certain (dis-) similarities through which they can be distinguished. An important criterion to do this is the so-called radio-loudness, which was introduced by Kellermann et al. (1989) and is defined as the ratio of radio to optical flux

$$R_L = \frac{F_R}{F_O}, \quad (1.1)$$

where the radio flux F_R is measured at 5 GHz and the optical flux F_O is determined in the B-band. Sources with $R_L \lesssim 1$ are considered to be radio-quiet, while sources with $R_L > 10$ are said to be radio-loud. According to them, approximately 15% of all AGN are radio-loud.

Another distinction is based on the optical and ultraviolet spectra of AGN, more specifically on the presence or absence of narrow and broad emission lines. These emission lines are produced in clouds

¹For comparison: the luminosity of the Sun is $L_{\odot} \approx 10^{33}$ erg/s $\approx 10^{26}$ W

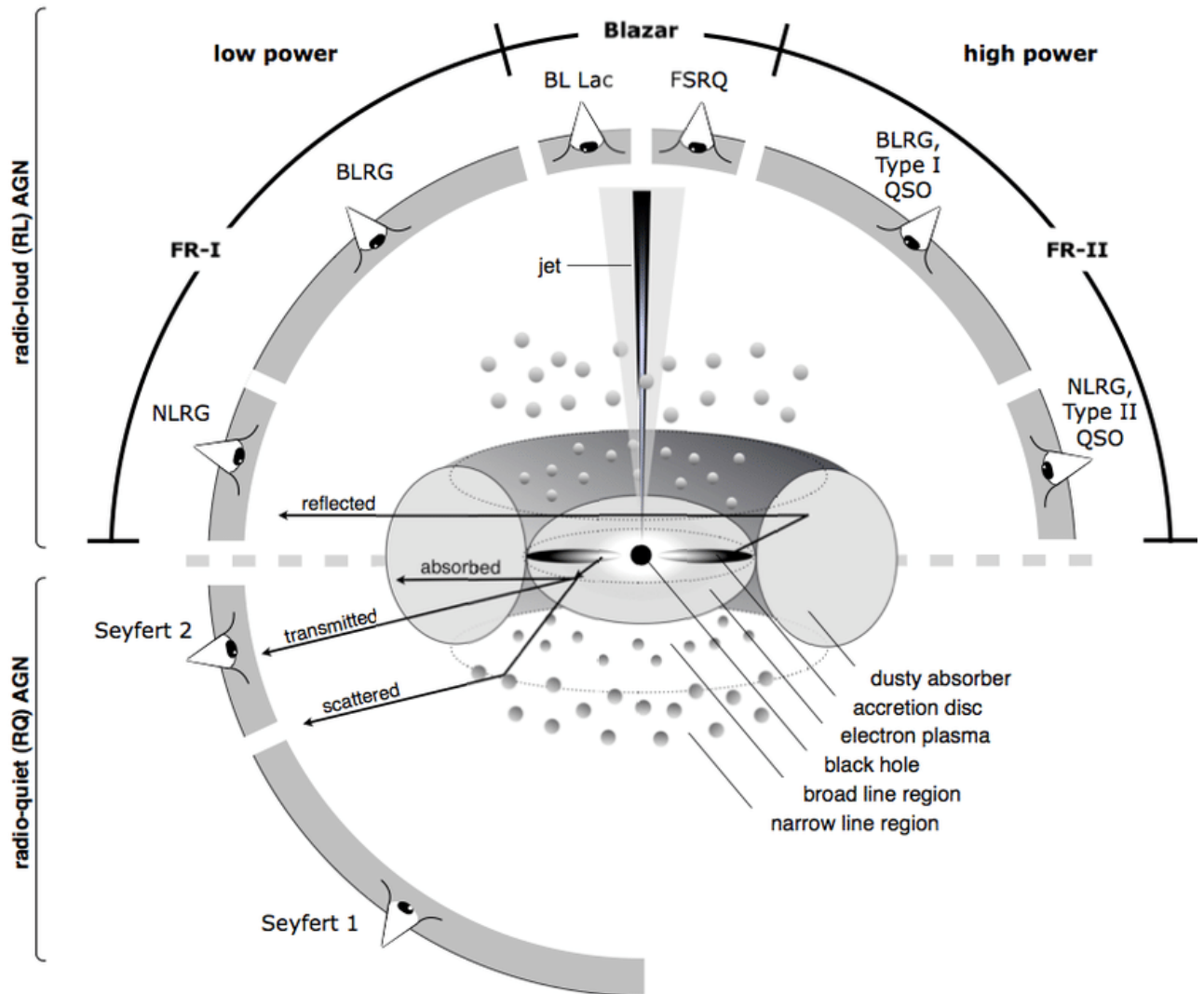


Figure 1.1: The unified scheme of AGN, taken from Beckmann & Shrader (2012). AGN are divided into radio-loud and radio-quiet, depending on their ratio of radio to optical flux. This roughly translates into the presence or absence of a jet. Different classifications arise depending on the viewing angle.

of gas, where photons are caught in an excited state and return to a configuration with lower energy. Besides the permitted narrow emission lines, even forbidden narrow lines can be observed. These transitions typically do not appear on Earth, as the excited atoms would collide with another particle before the spontaneous decay could happen. On the contrary, the mean free path in the gas clouds is much longer, such that the low probability transitions can occur. Additionally, broad emission lines can also be observed. The classification now divides AGN in type 1 and type 2, where type 1 AGN show both broad and narrow emission lines and have a bright continuum, and type 2 AGN only have narrow emission lines and a weak continuum.

According to the unified scheme (Urry & Padovani, 1995), all phenomena linked to AGN can be tied to the same type of object, the SMBH in the center of every AGN, with $M_{\text{SMBH}} = 10^6 - 10^9 M_{\odot}$ (Woo & Urry, 2002). The different properties mentioned above can now be explained by considering the angle to the line-of-sight. The SMBH accretes matter onto a so-called accretion disk. Clouds with different properties, such as their density, are responsible for the observed broad and narrow emission lines. Depending on their emitted lines, they are called the broad line region (BLR) and narrow line region (NLR). As forbidden lines can only be observed for narrow lines, the NLR has to have a lower density

than the BLR. The broad lines are a consequence of the BLR being closer to the SMBH than the NLR, so that the atoms in the clouds each experience a peculiar Doppler shift that, added together, results the lines broadening. Surrounding the black hole as well as the BLR is a dusty torus, blocking their emission features for certain angles to the line-of-sight. Note that recent studies like [Vollmer et al. \(2018\)](#) and [Hönig \(2019\)](#) used mid-infrared interferometry to resolve the dust structures in nearby AGN and concluded that the infrared emission originates in two components, a disk and a hollow cone, rather than a torus shape. Radio-loud AGN also feature highly energetic plasma outflows, perpendicular to the accretion disk, called jets, emitting their radiation in the radio regime. Figure 1.1 illustrates the components mentioned above and gives the names of the different types of AGN according to their properties.

The for this work relevant AGN are all observed with small angles to the line-of-sight and are called blazars. They do not exactly fit into the type 1/2 categorization, as they are typically lacking strong optical emission lines and show strong continuum variability as well as polarization in their optical spectra. Additionally, although they are radio-loud, no extended emission in the form of a jet can be seen. The blazar class can further be divided into BL Lac objects and flat spectrum radio quasars (FSRQ). While BL Lacs show properties similar to their prototype BL Lacertae, i.e., no strong optical emission lines or are even completely featureless, FSRQs, however, do show strong broad emission lines ([Urry & Padovani, 1995](#)).

1.2 The blazar sequence

Blazars typically are the most luminous type of AGN. This is due to Doppler boosting, as the particles in the jet move at highly relativistic velocities. Considering the relativistic Doppler factor $\delta = 1/(\Gamma(1 - \beta \cos \theta))$, where $\beta = v/c$ is the velocity in units of the speed of light, $\Gamma = (1 - \beta^2)^{-1/2}$ is the Lorentz factor and θ is the angle between the velocity vector and the line-of-sight, the luminosity of a single blob, where a blob represents some inhomogeneity propagating along a jet, transforms as

$$L_{\text{obs}} = \delta^4 L'_{\text{blob}}. \quad (1.2)$$

Therefore, even relatively small relativistic velocities can inflict a boost by a factor of 1000 ([Sikora et al., 1997](#)). Relativistic beaming also explains the one-sidedness of jets that is often observed, as the luminosity of the jet facing away from the observer is dampened by the same factor.

To get an overview of the broadband behavior of blazars, it is useful to take a look at their spectral energy distribution (SED), which illustrates how the flux F changes with respect to the frequency ν . In a standard SED plot, the flux density is multiplied by the corresponding frequency νF_ν and is plotted on a logarithmic scale. Here, the integrated area under the graph represents the emitted power in a certain frequency range. A typical SED of a blazar, showing the characteristic double hump structure, is shown in Fig. 1.2 on the example of Mrk 421.

As the radiation associated with the low frequency peak shows polarization features, it is thought to be produced by synchrotron emission, i.e., by charged particles gyrating at relativistic velocities through magnetic fields. While the synchrotron peak is generally accepted, the origin of the high frequency peak is not as clear. Most models describe the peak via inverse Compton (IC) scattering of photons, although it is not yet evident if these photons are the synchrotron photons themselves or external photons from the accretion disk, the BLR or the torus (see [Ghisellini et al., 1998](#), and references therein). Additionally, [Mannheim \(1993\)](#) proposed that the high frequency peak could also be described by hadronic processes.

In their study, [Fossati et al. \(1998\)](#) used three complete samples of blazars and computed the average SED from the radio to the γ -ray band for each complete sample and for groups of blazars binned together according to their radio luminosity. They found what is now known as the „blazar sequence“. Based on this work, [Donato et al. \(2001\)](#) developed the sample by adding X-ray data. A plot of the

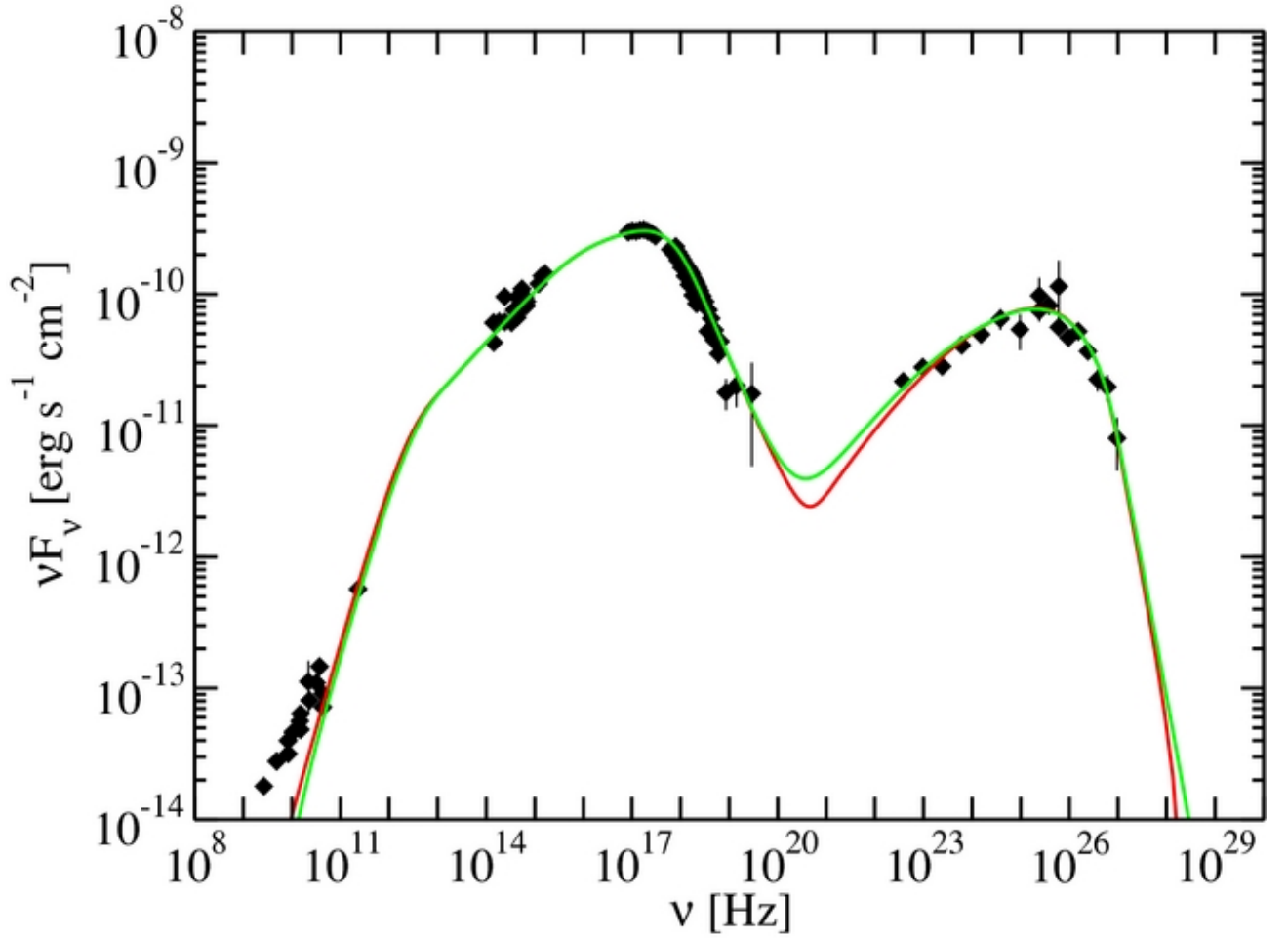


Figure 1.2: Spectral energy distribution (SED) of Mrk 421 showing a typical double hump structure (Abdo et al., 2011). The low frequency peak is generally attributed to synchrotron emission, while the peak at high frequencies most probably arises from inverse Compton scattering.

average blazar SEDs is shown in Fig. 1.3. Their results will be shortly summarized in the following. All SEDs show two peaks, where the first (synchrotron) peak is anticorrelated with the source luminosity and the second (IC) peak also moves to lower frequencies. Actually, the ratio between the two peak frequencies is constant when comparing the analytical curves. The last major finding is the strength of the second peak being proportional to the luminosity, i.e., the brighter a source, the more its γ -ray emission dominates. However, it has to be noted that there is a bias in the high-energy data, as they were preferentially detected during outbursts, and that there are a small number of sources that do not fit the sequence. Note also that [Giommi et al. \(2012\)](#) proposed a „simplified scenario“, completely alternative to the blazar sequence. They claim that the sequence is only a result of selection effects. [Ghisellini et al. \(2017\)](#) used the complete flux-limited sample of blazars with known redshifts detected by the *Fermi* satellite and binned the data according to their γ -ray luminosity. Compared to the original blazar sequence, their sequence shows less Compton dominance, a different γ -ray slope at low luminosities and a more abrupt change of the synchrotron peak. The differences between the two models can be explained by the fact that *Fermi* can also detect blazars that are currently not flaring, as was the case with its predecessor EGRET.

1.3 High-peaked BL Lacs

[Padovani & Giommi \(1994\)](#) introduced the distinction between high-peaked BL Lacs (HBLs) and low-peaked BL Lacs (LBLs), where the dividing line between the two classes is at a flux ratio $f_x/f_r \sim 10^{-11}$ with the X-ray flux f_x in $\text{erg s}^{-1} \text{cm}^{-2}$ and the radio flux f_r in Jansky. This corresponds to HBLs having their primary emission hump at $\nu \geq 10^{15}$ Hz, while LBLs have $\nu < 10^{14}$ Hz and intermediate-peaked BL Lacs (IBLs) have their emission peak in between.

As described in the section above, blazars are found to emit at higher and higher energies the fainter they are, shifting their emission peaks into the X-ray and TeV γ -ray regime. So-called „extreme blazars“ can even show the peaks shifted upwards by two orders of magnitude ([Biteau et al., 2020](#)). Although they are plentiful, they can only be observed in the near universe, because their luminosity is rather low. There are two different kinds of extreme blazars: the ones that show extreme-synchrotron emission and the ones that are extreme-TeV emitters, having a γ -ray peak above $h\nu \geq 1 \text{ TeV}$ ($\sim 10^{26}$ Hz). Additionally, there are three types of extreme behavior, illustrated in Fig. 1.4. [Biteau et al. \(2020\)](#) classify them as objects that become extreme during flares, where both peaks shift to higher energies and back again, objects that show a constant hard synchrotron spectrum, but no hard TeV spectrum, and objects that show a steady hard γ -ray spectrum which peaks above several TeV.

Since their emission peaks at very high frequencies, extreme blazars are typically fairly faint in the radio regime (see also Fig. 1.3), making it difficult to observe them with standard radio telescopes. See Sect. 3 for an explanation on how these sources were observed, why this specific telescope was chosen and, finally, how the data got reduced.

1.4 Doppler crisis

The following section is mainly based on [Piner & Edwards \(2015\)](#) and all references therein, where not else specified.

An important characteristic of AGN is their flux variability in all spectral bands. Especially the radio variability can be used to detect active periods on parsec scales. As already stated above, blazars can vary on the timescales of minutes ([Albert et al., 2007](#)), implying an upper limit for the size of the emitting region. Short timescale variability produces two contradictory problems that can be solved by assuming bulk relativistic motion towards the observer, reducing the intrinsic luminosity and the implied energy of photons and increasing the internal timescales. This requires a Doppler factor $\delta \geq 100$ ([Lyutikov & Lister, 2010](#)). The bulk Lorentz factor can actually be constrained by very-long baseline interferometry (VLBI) measurements of blobs moving with apparent superluminal speeds. VLBI works

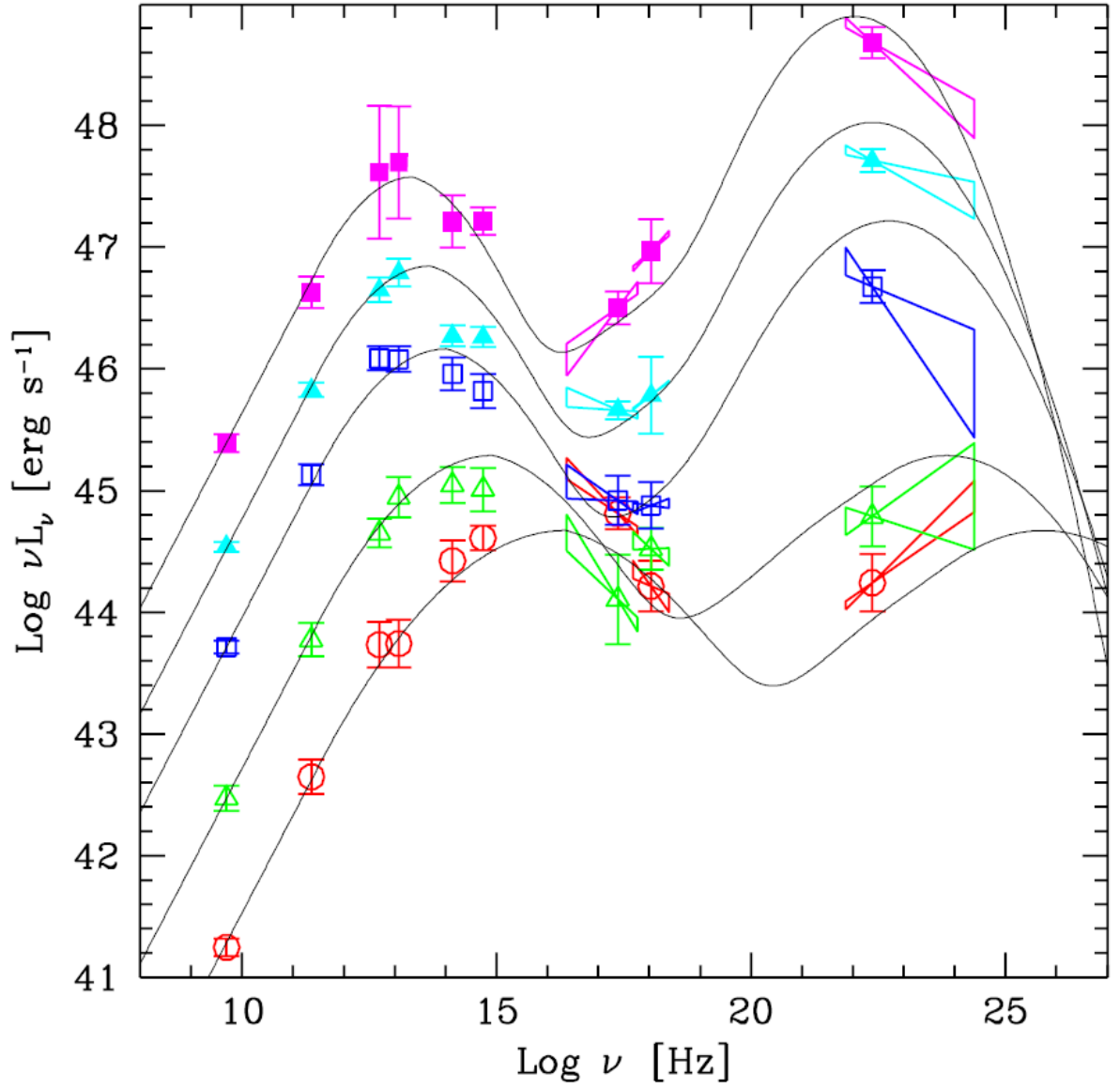


Figure 1.3: Average SEDs of blazars, binned according to their radio luminosity. The overlaid curves are the spectra constructed by [Donato et al. \(2001\)](#), based on the work of [Fossati et al. \(1998\)](#).

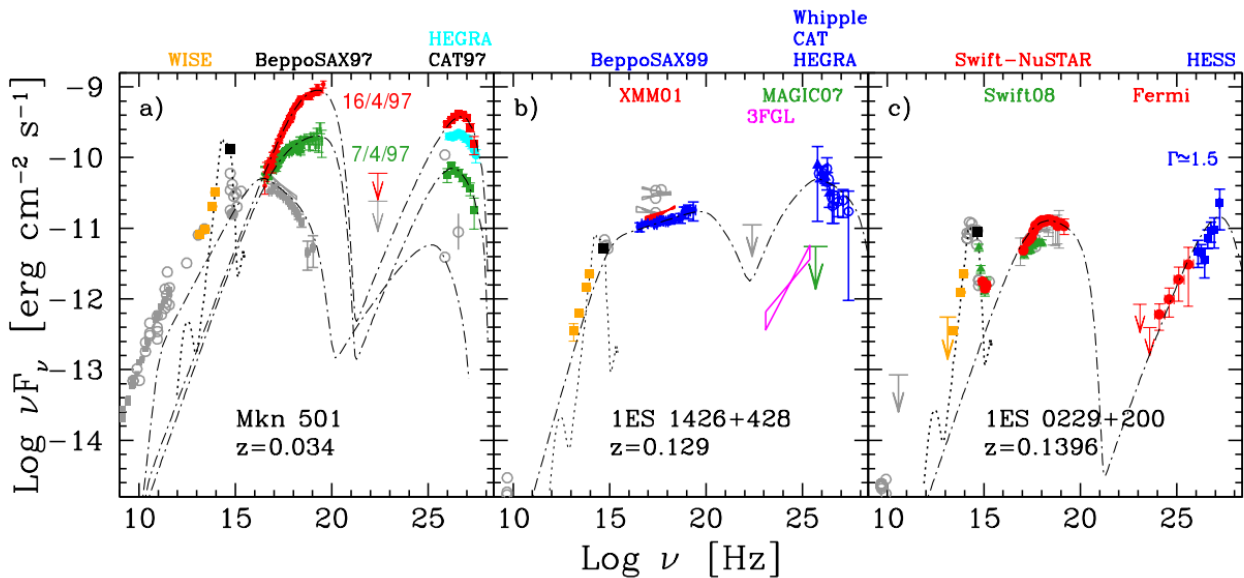


Figure 1.4: The three types of extreme blazar behavior, according to Biteau et al. (2020). Panels a) and b) show SEDs of extreme-synchrotron blazars that shift to higher energies during flares or have a stable hard synchrotron spectrum, respectively. Panel c) shows the SED of an extreme-TeV blazar, showing a persistent hard γ -ray spectrum.

by using radio telescopes all over the globe, reaching unprecedented angular resolutions and allowing observers to resolve the parsec-scale structures of AGN. Apparent faster-than-light motion happens when a blob is moving towards an observer with speed v under an angle θ with respect to the line-of-sight, emitting radiation at times t_0 and $t_1 > t_0$. As a projection effect, the apparent speed of the blob in the jet is

$$\beta_{\text{app}} = \frac{\beta \sin \theta}{1 - \beta \cos \theta}. \quad (1.3)$$

For small angles and speeds close to the speed of light, β_{app} can be greater than 1 with a maximum value of $\beta_{\text{app}} = \Gamma\beta$, when $\theta \cong 1/\Gamma$. Therefore, measuring β_{app} constrains the bulk Lorentz factor Γ , under the assumption that the blob movement corresponds to the underlying bulk motion of the jet. Interestingly, Piner & Edwards (2018) find a maximal 2σ apparent speed lower limit of $3.6c$, considering a sample of 38 TeV HBLs. Combining such slow apparent jet speeds with the high Doppler factor implied by the variability argument results in very small viewing angles of order $\theta \ll 1^\circ$ and therefore in unphysically small jet opening angles as well as huge linear sizes. Considering realistic viewing angles of a few degrees instead immediately favors modest Lorentz and Doppler factors. The discrepancy between the Doppler factors for HBLs arising from the different methods was coined the „Doppler crisis“.

A possible resolution to this crisis is the coexistence of multiple Doppler factors in the same jet, such that the radio and γ -ray emission is produced in different parts of the jet. Georganopoulos & Kazanas (2003) propose a model where the jet decelerates along its length. Alternatively, as formulated by Ghisellini et al. (2005), a jet structure with two main parts, the spine and the sheath, can also be used to explain the crisis. Here the spine is a highly collimated stream of matter, moving at relativistic speeds in the middle of the jet, surrounded by the slower moving sheath. The interaction of the spine with the sheath potentially results in Doppler boosting of the photons in the jet, amplifying the synchrotron and IC radiation, which could even explain the Compton dominance of certain sources. In fact, VLBI observations (see e.g., Ros et al., 2020) show strong signs of a spine-sheath structure.

2 | Introducing the sample

The sample of sources considered in this work is mainly based on the „TeV Effelsberg Long-term AGN Monitoring“ (TELAMON) program by Kadler et al., although it contains some additional sources that were added later into the program.

Table 2.1 shows the names and classifications of all sources in the sample as reported by the TeVCat¹ catalog and the NASA/IPAC Extragalactic Database (NED)². The J2000 names refer to the truncated right ascension and declination of the source in reference to the Julian standard equinox J2000, while the „common name“ is the one used by TeVCat.

Included are a total of 38 sources: 25 HBLs, with 11 of them being extreme blazars, 6 IBLs, 2 FSRQs, 2 radio galaxies and 3 sources of unknown/unclear type. With that, about two thirds of the sample are HBLs, while about one third are extreme blazars.

The original sample contained all 22 known TeV-emitting AGN at declination $\geq 30^\circ$ that have a low-state emission level in the range between 100 mJy and 400 mJy. Additionally, all types of extreme behavior, according to Biteau et al. (2020) (see Sect. 1.3), are represented in the sample.

Using the results of this thesis as well as following works on the Effelsberg monitoring program, the radio variability properties of these TeV sources will be characterized. A similar study was conducted by Lindfors et al. (2016), who studied the radio variability of very-high-energy gamma-ray emitting BL Lac objects based on 15 GHz flux-density measurements done by the OVRO³ program and compared them to data in the optical band. As most of the sources in our sample are also in the Tuorla blazar monitoring program⁴ that observes at optical frequencies, it is planned to extend their work by employing higher radio frequencies and using a more sensitive telescope, namely the Effelsberg 100 m radio telescope.

Angelakis et al. (2019) already used this telescope to observe the much better studied *Fermi* GeV blazars. Their work also laid the foundation of the analysis procedure described in Sect. 3.3. However, although their program is logistically similar to our TeV monitoring program, we will be able to go to a statistical comparison of extreme blazars and other TeV-emitting AGN for the first time.

Piner & Edwards (2018) already did a study on HBLs, although, they used the Very Long Baseline Array (VLBA)⁵ to image them on the parsec scale in multiple epochs. They analyzed the apparent speeds of jet components and found that most of them are consistent with no motion on a 2σ level, while the lower limit of the highest apparent speed on the same level is $3.6c$. Radio variability data obtained in this thesis and the monitoring program will, in the future, be complemented by VLBI observations of a sub-sample of the sources. The variability data can be used to connect and interpret the VLBI observations. With this, the proposed multi zone models in Sect. 1.4 can be further investigated.

¹<http://tevcat.uchicago.edu/>

²<https://ned.ipac.caltech.edu/>

³<https://www.ovro.caltech.edu/>

⁴<https://users.utu.fi/kani/1m/>

⁵<https://public.nrao.edu/telescopes/vlba/>

Our sample contains some well-known sources such as Mrk 421, which is one of the closest blazars to Earth and also one of the most observed sources in the gamma-ray regime, and TXS 0506+056, which is the first known source of high-energy astrophysical neutrinos (Padovani et al., 2018). Additionally, two sources, namely PKS 1256+018 and 4FGL J0658.6+0636, were included as they were reported to be positionally coincident with newly detected high-energy IceCube neutrinos (see ATel#14177⁶ and ATel#14188⁷). Both sources were observed soon after the detection and the results were reported in ATel#14191⁸ (and ATel#14194⁹). The latter of those sources is now a confirmed very-high-energy emitting blazar (see ATel#14200¹⁰). Finally, BL Lacertae is included as a bright reference source.

Compared to other monitoring programs such as Metsähovi¹¹ or OVRO, which do not yield data of reliable quality for source flux densities of $\lesssim 400$ mJy, the Effelsberg telescope can produce high-quality data for even weaker sources, as will be discussed in Sect. 3.

⁶<http://www.astronomerstelegam.org/?read=14177>

⁷<http://www.astronomerstelegam.org/?read=14188>

⁸<http://www.astronomerstelegam.org/?read=14191>

⁹<http://www.astronomerstelegam.org/?read=14194>

¹⁰<http://www.astronomerstelegam.org/?read=14200>

¹¹<https://www.aalto.fi/en/metsahovi-radio-observatory>

Name J2000	Common Name	Class ^a
0035+5950	1ES 0033+595	HBL
0112+2244	S2 0109+22	IBL
0214+5144	TXS 0210+515	HBL
0222+4302	3C 66A	HBL
0232+2017	1ES 0229+200	HBL*
0303-2407	PKS 0301-243	HBL
0316+4119	IC 310	unknown
0416+0105	1ES 0414+009	HBL*
0507+6737	1ES 0502+675	HBL
0509+0541	TXS 0506+056	IBL/HBL/FSRQ
0521+2112	RGB J0521+212	IBL
0650+2502	1ES 0647+250	HBL
0658+0637	4FGLJ0658.6+0636	HBL
0955+3551	3HSP J095507.9+35510	HBL*
1015+4926	1ES 1011+496	HBL
1104+3812	Mrk 421	HBL*
1136+7009	Mrk 180	HBL
1145+1936	3C 264	RG
1217+3007	ON 325	HBL
1221+2813	W Comae	IBL
1221+3010	1ES 1218+304	HBL*
1230+2518	ON 246	IBL
1259+0136	PKS 1256+018	RG
1422+3223	OQ 334	FSRQ
1427+2348	OQ 240	HBL
1428+4240	1ES 1426+428	HBL*
1443+2501	PKS 1441+25	FSRQ
1518-2731	TXS 1515-273	HBL
1555+1111	PG 1553+113	HBL
1653+3945	Mrk 501	HBL*
1728+5013	I Zw 187	HBL*
1743+1935	1ES 1741+196	HBL*
1813+3144	B2 1811+31	IBL
1959+6508	1ES 1959+650	HBL*
2018+3851	TXS 2016+386	unknown
2158-3013	PKS 2155-304	HBL
2202+4216	BL Lac	IBL
2347+5142	1ES 2344+514	HBL*

Table 2.1: Sample of all sources considered for this work. Source classifications and common names are based on the TeVCat catalog and the NED. Sources with more than one or unknown classification cannot be unambiguously attributed to one class yet. J2000 names are truncated right ascension and declination of the source.

^a FSRQ: flat spectrum radio quasar, RG: radio galaxy, IBL: intermediate-peaked BL Lac, HBL: high-peaked BL Lac (extreme blazars are denoted as HBL*)

3 | Observations and data reduction

As most matter is optically thin for radio waves, they can reach Earth without being absorbed or scattered. This gives radio astronomy a critical advantage over, e.g., gamma-ray astronomy, as it can be done from the ground, rather than needing satellites in space. Earth's atmosphere presents an opaque barrier to most of the electromagnetic radiation, with the exception of the so-called atmospheric windows in the optical and the radio regime. Here, radiation can pass through the atmosphere and reach the ground, where it can be observed by telescopes. A plot of the atmospheric transmittance is shown in Fig. 3.1. The low wavelength end of the radio window is due to molecules in the atmosphere such as CO₂, O₂ or H₂O absorbing incoming radiation with $\lambda \leq 1$ mm. Conversely, the long wavelength limit arises as Earth's ionosphere reflects radio waves longer than $\lambda \sim 30$ m.

The important quantity of a source is its flux density S_ν , i.e., its emitted power per unit solid angle and frequency. As the flux densities for radio observations are typically quite weak, they are usually reported in the non-SI unit jansky, where $1 \text{ Jy} = 10^{-26} \text{ Wm}^{-2}\text{Hz}^{-1}$. The unit is named after the American physicist Karl G. Jansky who is thought of as the founding father of radio astronomy, as he first discovered radio waves emitted by the Milky Way.

3.1 The Effelsberg 100m telescope

All sources considered in this work were observed by the Effelsberg 100 m telescope. The following section is based on information from the IVS biennial report¹ and the data sheet² of the telescope, provided by the Max-Planck-Institut für Radioastronomie (MPIfR), who also operate the telescope. It is one of the largest fully steerable single-dish radio telescopes in the world and is located in a protected valley in Effelsberg, Germany, near Bonn. Its instruments can observe celestial objects in a range of wavelengths from 1 m (300 MHz) down to 3.5 mm (90 GHz). For this work, data were recorded at $\lambda = 1.3$ cm and $\lambda = 7$ mm. The main dish is a paraboloid with a diameter of 100 m and a surface accuracy (rms) of $\sigma \sim 0.5$ mm. The telescope can be rotated about two perpendicular axes, one vertical and one horizontal. While the rotation about the vertical axis varies the azimuth, the rotation about the horizontal axis varies the altitude or angle of elevation of the pointing direction. For measuring purposes, the telescope has a maximal field of rotation from 33.5° to 506.5°, where 0° is north, and can be tilted between 8.1° to 89°. As the telescope moves, the main dish will be deformed due to gravity, which results in the loss of the defined parabolic form. To counteract this problem, it was build using the principle of homology, meaning the reflector will always have a parabolic shape with a well defined focal point. This focal point, however, may change with different degrees of tilt, so the parabolic shape of the reflector is always different as well.

The angular resolution θ of a telescope describes how well it can distinguish between two small features of an object. In other words, two objects that are separated by an angle smaller than the angular

¹<https://ivscc.gsfc.nasa.gov/publications/br2017+2018/nseffelsberg.pdf>

²<https://www.mpifr-bonn.mpg.de/231173/specs>

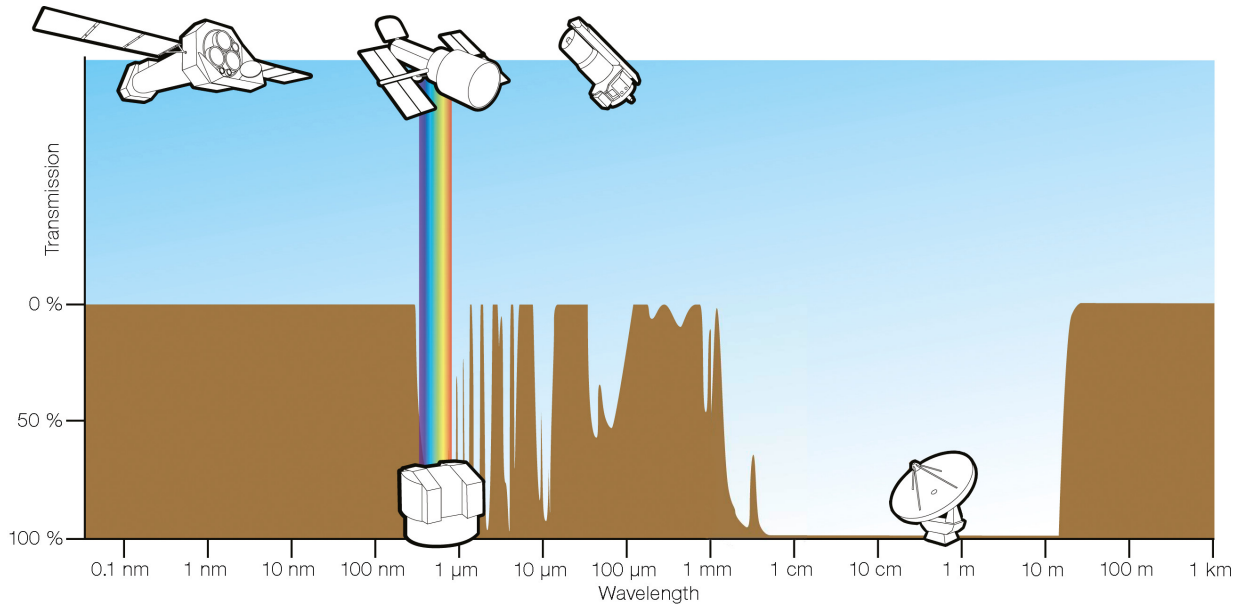


Figure 3.1: The brown curve shows the transparency of Earth’s atmosphere at a given wavelength to radiation from space. There are two major atmospheric windows, located at visible and radio wavelengths, where radiation can reach the ground. Credit: ESO/https://www.eso.org/public/images/atm_opacity/

resolution of the telescope can not be told apart. This resolution is limited by the Rayleigh criterion

$$\theta \approx \frac{\lambda}{D}, \quad (3.1)$$

where D is the diameter of the telescope and λ is the observing wavelength. Let $\lambda = 1.3$ cm and $D = 100$ m, then the Effelsberg telescope would observe at a resolution of $\theta_E \approx 0.5$ arcmin. In contrast, the human eye has a resolution similar to 1 arcmin. As is evident from Eq. 3.1, the angular resolution decreases with smaller dishes and increases with larger ones. However, there is an economical limit to the size of single-dish telescopes. Nevertheless, even higher resolutions can be achieved by utilizing very-long baseline interferometry (VLBI), where multiple telescopes, potentially situated all over the world, are used to produce images of the same angular resolution as an instrument with an effective diameter of the largest separation between two telescopes would have.

Another useful measure for a telescope is its sensitivity Γ , which relates the measured temperature in Kelvin to the flux density in jansky. The sensitivity for a specific wavelength λ can be calculated by the Ruze equation following

$$\Gamma = \eta_A \Gamma_0 = \eta_A \frac{A_{\text{geo}}}{2k_B} = \eta_A \frac{\pi D^2}{8k_B} = \eta_A \cdot 2.844 \text{ K/Jy}, \quad (3.2)$$

where $D = 100$ m was used for the Effelsberg telescope, k_B is the Boltzmann constant, A_{geo} is the geometric area of the antenna and η_A is the aperture efficiency calculated by

$$\eta_A = \eta_0 \cdot \exp \left(-0.78 \left(\frac{4\pi\sigma}{\lambda} \right)^2 \right) \quad (3.3)$$

with σ the rms of the reflector. Using $\eta_0 = 0.55$, the theoretical sensitivity of the Effelsberg telescope at $\lambda = 1.3$ cm is $\Gamma \sim 1.25$ K/Jy (Bach et al., 2007). Here, the factor $A = 0.78$ is the Ruze loss correction factor for the Effelsberg telescope that describes the amount of curvature the reflector has and can vary between 0 and 1 (Ruze, 1966).

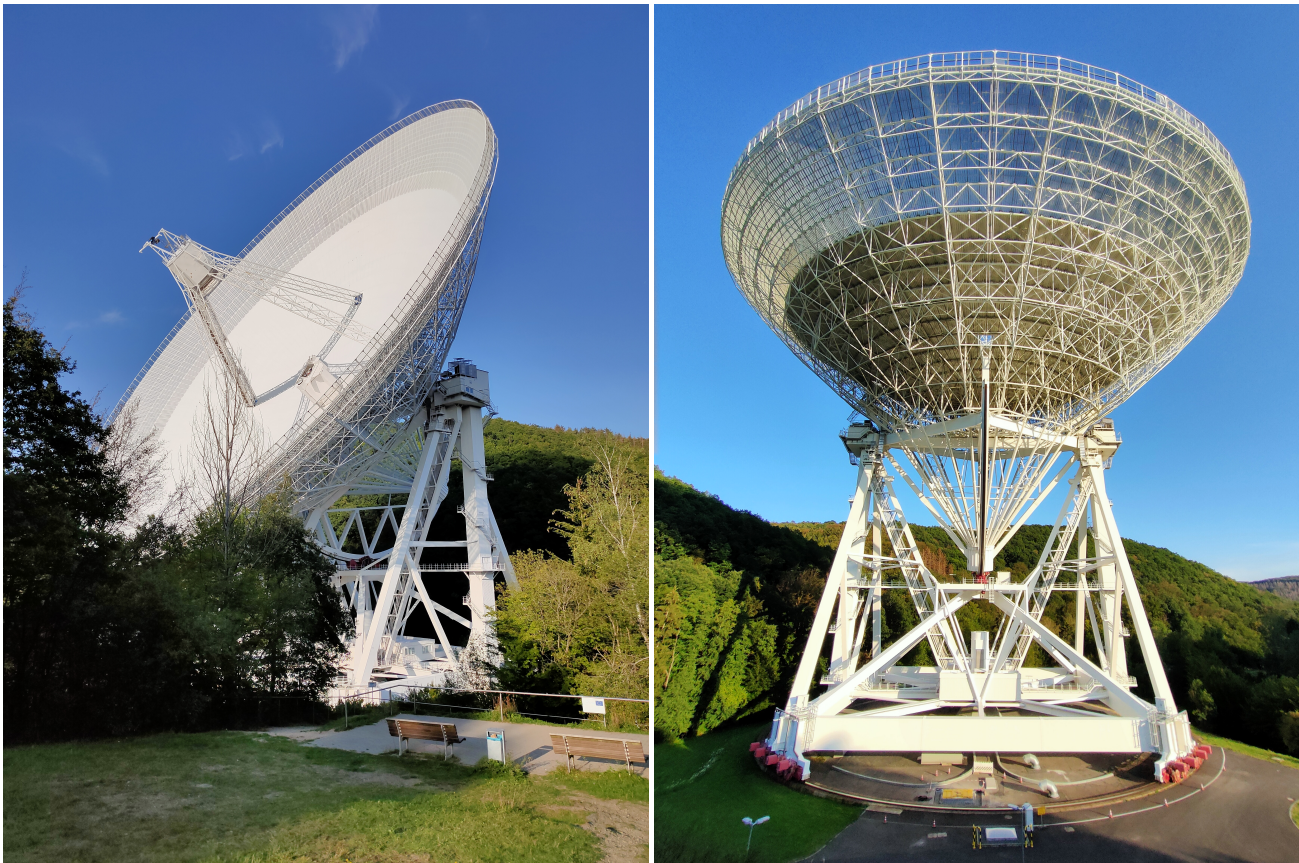


Figure 3.2: The Effelsberg 100 m telescope, located in Effelsberg, Germany, is one of the largest steerable single dish radio telescopes on Earth. With its 100 m dish it achieves high sensitivities and high angular resolutions.

Photographs: Jonas Heßdörfer, 2020

Therefore, considering Eq. 3.1 and Eq. 3.2, the larger the diameter of a telescope is, the better its resolution and the higher its sensitivity. Since most sources considered in this work are HBLs or extreme blazars, which are fairly faint radio sources, as explained in Sect. 1.3, they are typically not measurable by normal radio telescopes. However, the large dish of the Effelsberg 100 m telescope makes the observation of such sources possible, as it allows for high angular resolutions and high sensitivities. While the telescope is often used for spectroscopy or pulsar observations and it even participates in VLBI measurements, the important observation mode for this thesis is the one for pointed flux density measurements.

3.2 Observing with the Effelsberg telescope

All measurements were conducted using the secondary focus receivers „S14mm Double Beam RX“ at a wavelength of 1.3 cm and the „S7mm double beam RX“ at a wavelength of 7 mm. Each receiver delivers the data in four bands of frequencies centered around 19.25 GHz, 21.15 GHz, 22.85 GHz, 24.75 GHz and 36.25 GHz, 38.75 GHz, 41.25 GHz, 43.75 GHz, respectively. Actually, both receivers come with two horns, where the first horn acquires the radiation and passes it on to the receiver itself, and the second horn is used as a „weather horn“, as it does not observe the source itself but the atmosphere off-source, so that its measurements can be subtracted from the ones of the first horn to get rid of the effects of bad weather, as will be described in the next section.

For the monitoring program, the sources were observed in intervals of two to four weeks, dynamically scheduled depending on the current weather. The following describes the basics of one such observa-

tional run.

As all sources can be seen as point-like, the observations were done using so-called „cross-scans“, meaning the telescope response is recorded while it is repeatedly slued over the source position. This happens in two orthogonal directions, where one slue in one direction is called a „sub-scan“. The directions of the scans are azimuthal (AZI) and in elevation (ELV), i.e., in longitude and latitude, respectively. For the S14 receiver, a total of two scans with eight sub-scans each were employed. This includes all four 1.3 cm frequencies. On the contrary, the S7 receiver was used in a different way. Here, 36.25 GHz and 38.75 GHz are measured with two scans of eight sub-scans, too, but 41.25 GHz and 43.75 GHz are measured as one scan with 16 sub-scans. Overall, using the S14 and S7 receiver as described above, a standard observation of a single source takes ~ 30 minutes.

An important thing to note here is the fact that most sources are not visible all the time, but rather rise and fall across the horizon as an effect of Earth’s rotation, and only a few sources are circumpolar. As a consequence, the order in which the sources are observed has to be planned carefully so that as many sources as possible are observed during a session. Furthermore, it would be optimal to observe each source at a high elevation, as the atmosphere has less influence on the signal there. Observing a source at low elevation near the horizon should be avoided, since ambient light could influence the measurement. A few sources in the sample actually do not noticeably rise above the horizon at Effelsberg at all, as their declinations are quite low. Luckily, there is a valley in the Effelsberg horizon, where these sources are visible for around two hours every day. Nevertheless, catching them without completely disrupting the scheduled observations is often not possible or only hardly manageable.

In addition to the sources of the sample, calibration sources were also observed. As their flux densities are well known, they can later be used to convert the observed antenna temperature T_A into Jy. The antenna temperature is defined as the equivalent temperature of a hypothetical resistor, which would generate an output noise of the same spectral power as the recorded signal P_{rec} , and follows

$$P_{\text{rec}} = k_B T_A, \quad (3.4)$$

where k_B is the Boltzmann constant. What the telescope actually measures is the system temperature T_{sys} , which is the antenna temperature in an idealized experiment in which the receiver noise, influences of background noises and all other sources of noise, but no target source, are considered. The system temperature is then simply the sum of all the noise temperatures. Using T_{sys} in Eq. 3.4 results in the total noise power of the system.

Several calibrators were observed in each observing session, one at the beginning, preferably one at the end and depending on the length of a session, several more calibrators in between. A plot of known calibrators and their flux densities is shown in Fig. 3.3, although not all of them were used. Speaking from experience, sources like 3C 48 and 3C 295, which have flux densities ≤ 0.5 Jy in the S7 range, are only suitable to a limited degree there, as they are relatively weak already and sometimes do not result in good scans. Additionally, 3C 48 and 3C 147 currently show variable spectra, making them less suitable for calibration purposes. When Ott et al. (1994) published their list of useful calibrators, they already noticed that these two sources show variability on the order of a few percent. However, the now observed variability seems to be much higher and needs to be further quantified.

Throughout the observation, the focus of the telescope has to be checked, too, as it changes with temperature. A defocused telescope will measure weaker flux densities, as its beam gets bigger. Focus scans are done before the initial observation of the first calibrator and are repeated every ~ 3 hours or if the temperature changes rapidly. The best sources to focus on are either bright calibrators like NGC 7027, bright blazars like BL Lac or even planets like Mars and Uranus.

The weather plays an important role when observing at 7 mm and 1.3 cm. Although Earth’s atmosphere is transparent to radiation of these wavelengths (see Fig. 3.1), there are still different phenomena that hinder the propagation of the signal. As already described in the beginning of this chapter, molecules in the atmosphere absorb incoming radiation. One of these molecules, water vapor, even has a specific

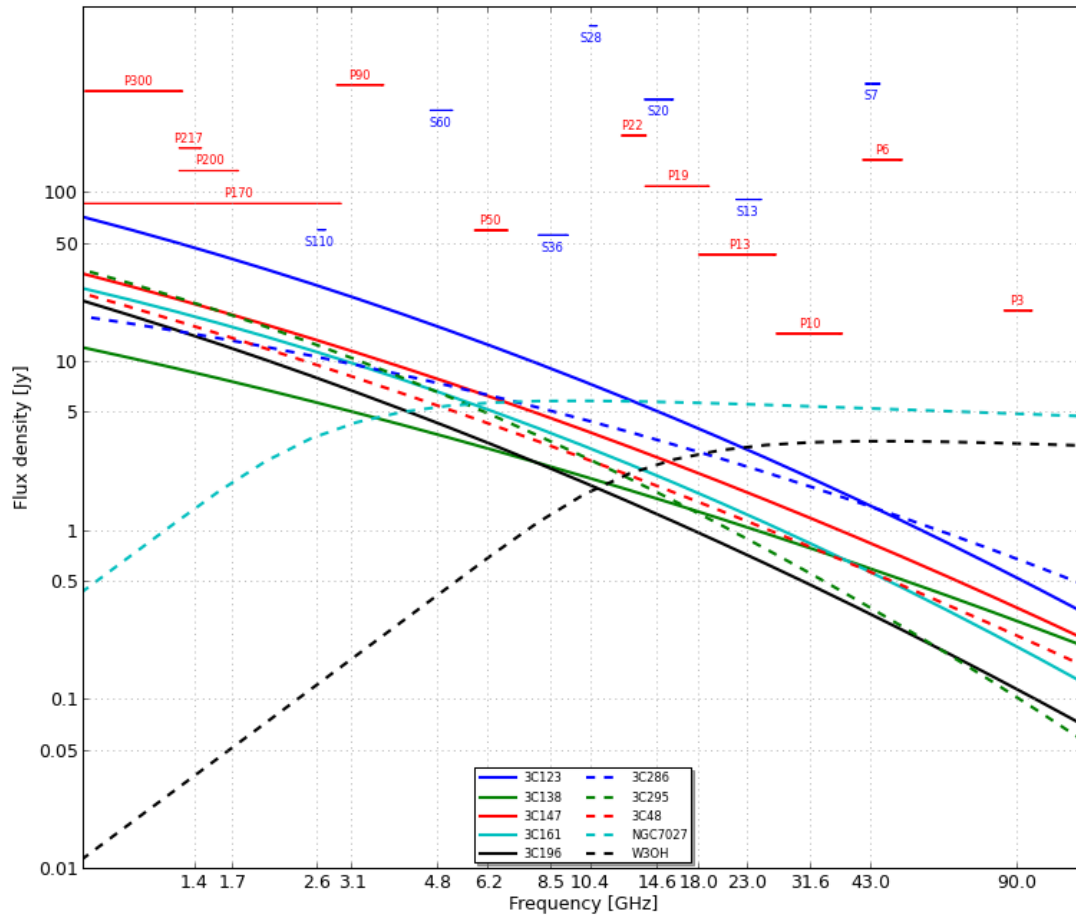


Figure 3.3: Plot of the flux densities of known calibrator sources as a function of frequency. The parts of the spectrum used for this work are marked at the top of the plot in blue by „S13“ and „S7“. Note that 3C 48 and 3C 147 currently show variability in their flux densities and can therefore not be used without caution. Taken from https://eff100mwiki.mpifr-bonn.mpg.de/doku.php?id=information_for_astronomers:user_guide:tips_calibrators

resonance peak at ~ 22 GHz, causing absorption. Using an ATM model of the atmosphere³ (Pardo et al., 2001), the absorption due to water vapor and the effects of the molecules at higher frequencies can be modeled. However, for realistic properties, their attenuation cannot explain the observed lack of a signal for bad weather conditions. While wind makes the telescope wobble and hydrosols (i.e., tiny raindrops of size ~ 0.1 mm) scatter radio waves following the Rayleigh scattering process, the main problem of bad weather are clouds. According to Kirchhoff’s law on thermal radiation, there is a direct relation between the absorption and the emission of electromagnetic radiation. For a system in thermal equilibrium, the amount of absorbed energy is equal to the re-radiated one. In the case of clouds in the atmosphere, they re-radiate the energy they gained from the Sun in the form of low temperature black body radiation. This thermal radiation then enters the receiver of the telescope and adds noise to the originally observed signal. Therefore, a strong cloud coverage completely hinders the detection of a source and makes observations pointless.

3.3 Data reduction of pointed flux measurements

After an observation, the data has to be reduced in order to receive the true flux density of the sources. The following section mainly follows the work of Angelakis et al. (2019) and the Calibration of the Effelsberg 100m telescope⁴ sheet.

While this section focuses on the theoretical aspects of the data reduction, a guide to the practical process of data reduction, using the computers and the software of the MPIfR, for new and experienced observers is given in appendix B.

As a first step, the quality of each scan was checked. A Gaussian is fitted to each individual sub-scan and the fits for all sub-scans in a direction are then subsequent averaged. Those scans with significant FWHM (here: half-power beam width HPBW) differences to the expected value, with large pointing offsets or with negative amplitudes are flagged and consequently further inspected. See Fig. 3.4 as an example. The top left plot is the original scan, an average over all longitude and latitude sub-scans. It was flagged because the longitude scan has a HPBW that is about one-twentieth of the latitude scan as well as having an offset of $-28''$. On the bottom of the figure all eight sub-scans making up the averaged scans are displayed. As can be seen, not all of them show reasonable Gaussian fits. The task now is to exclude bad sub-scans to improve the averaged scan to achieve a better Gaussian fit. Additionally, individual sub-scans showing radio frequency interference (RFI) should always be removed, as their high noise level negatively influences the fit and the averaging. Should no good fit be possible at all, the entire scan can be excluded from all further analysis. It turns out that excluding sub-scan 1 (due to RFI) and sub-scan 6 in the example results in the best possible average fit for this scan, shown in the top right. Now the two scans have comparable offsets, amplitudes and HPBWs. It should be noted that the scans shown in the figure are typical scans of weak but well detectable sources. For strong sources the fits follow the signal very well and the noise is much lower, while for weaker sources the noise is higher and the fits are generally worse.

Here the weather horn also comes into play. For non-optimal weather conditions, subtracting the second horn from the primary one can further improve the scan; an example for this is shown in Fig. 3.5. After the subtraction higher amplitudes and better Gaussian behavior of the signal and the fit are achieved.

After the initial quality check of the scans, there are several further steps to be done to arrive at the

³see e.g., <https://almascience.eso.org/about-alma/atmosphere-model> for the site of ALMA. Modeling a cloudy atmosphere can be done with https://mrs.eecs.umich.edu/codes/Module8_10/Module8_10.html, however, their parameters are too extreme for realistic cases.

⁴https://eff100mwiki.mpifr-bonn.mpg.de/lib/exe/fetch.php?media=information_for_astronomers:user_guide:effcalshort.pdf

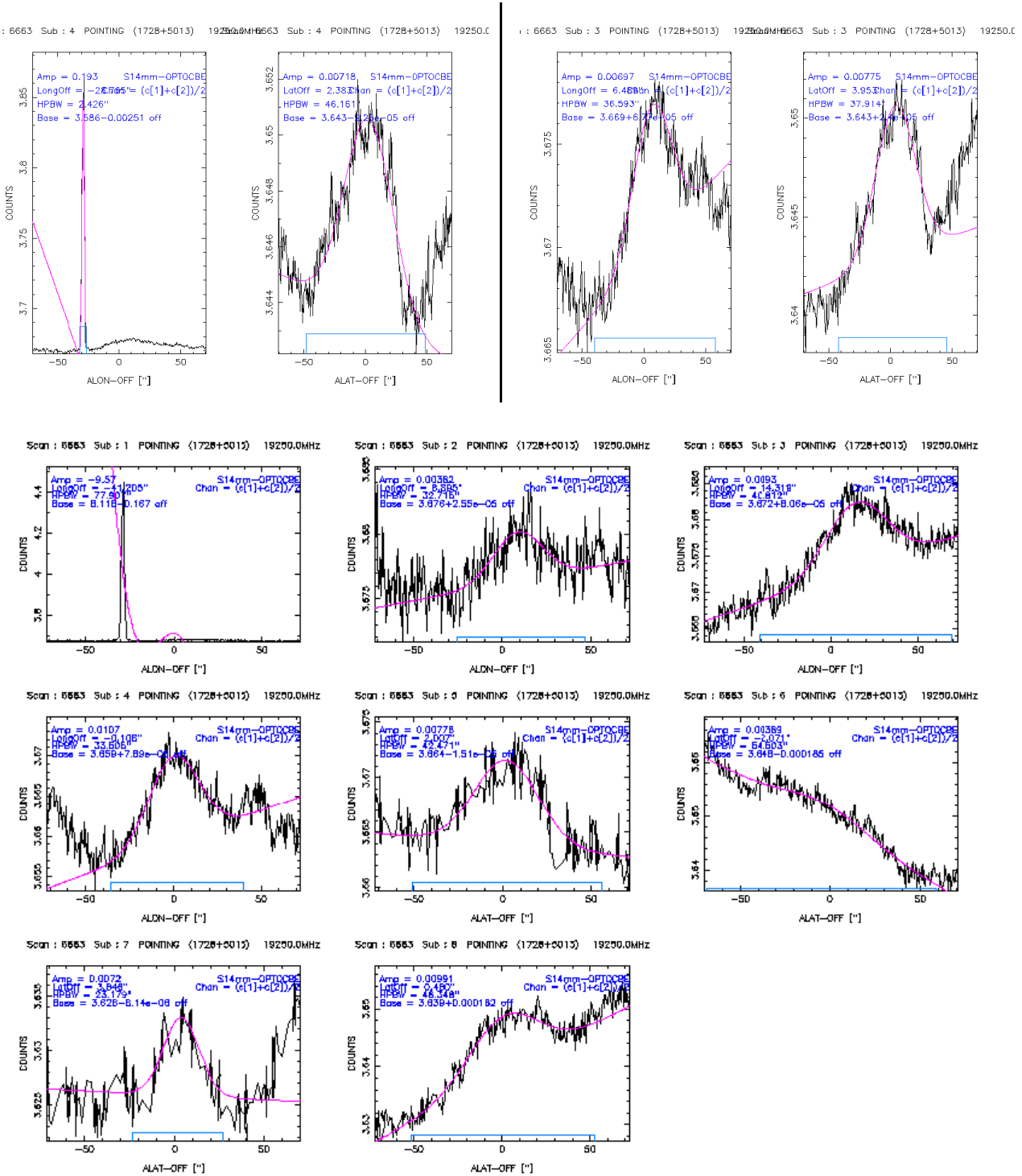
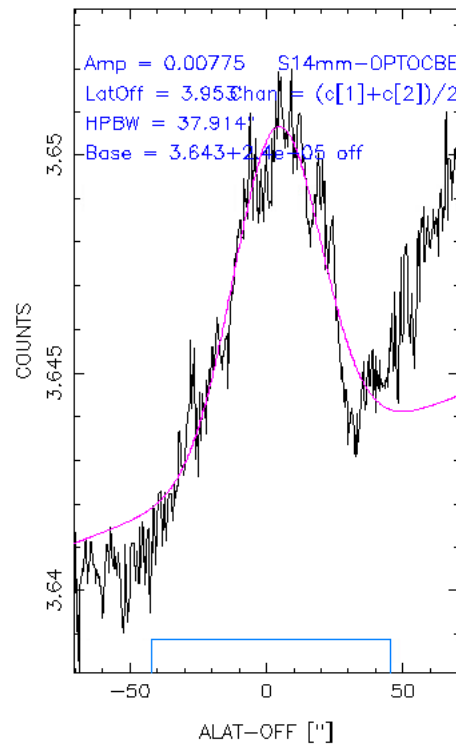
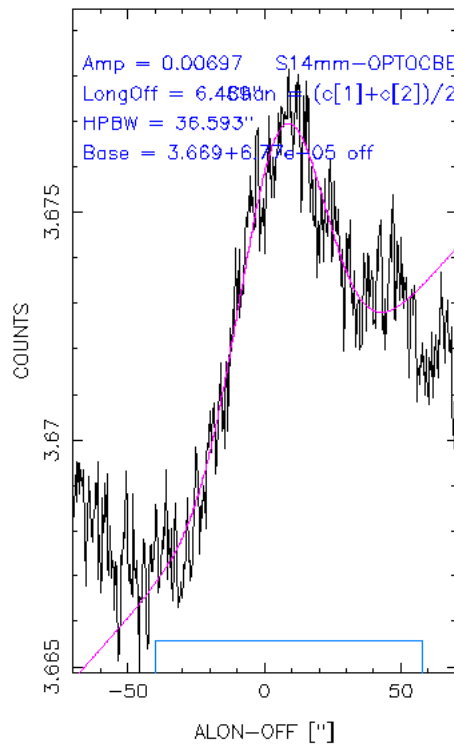


Figure 3.4: An example of how flagging works and the effect of excluding bad sub-scans. *Top left:* Average over all longitude and latitude sub-scans. Flagged for having a small HPBW and a big pointing offset. *Bottom:* All sub-scans that were done for this specific source and frequency. Not all Gaussian fits are reasonable and one sub-scan even shows radio frequency interference. *Top right:* Average over all sub-scans, excluding sub-scans 1 and 6. The HPBWs, the pointing offsets and the amplitudes of the longitude and latitude scans are now comparable and overall show a better Gaussian fit.

1 : 6663 Sub : 3 POINTING (1728+5013) 19250.0 19250.0 19250.0
 1 : 6663 Sub : 3 POINTING (1728+5013) 19250.0 19250.0 19250.0



1 : 6663 Sub : 3 POINTING (1728+5013) 19250.0 19250.0 19250.0
 1 : 6663 Sub : 3 POINTING (1728+5013) 19250.0 19250.0 19250.0

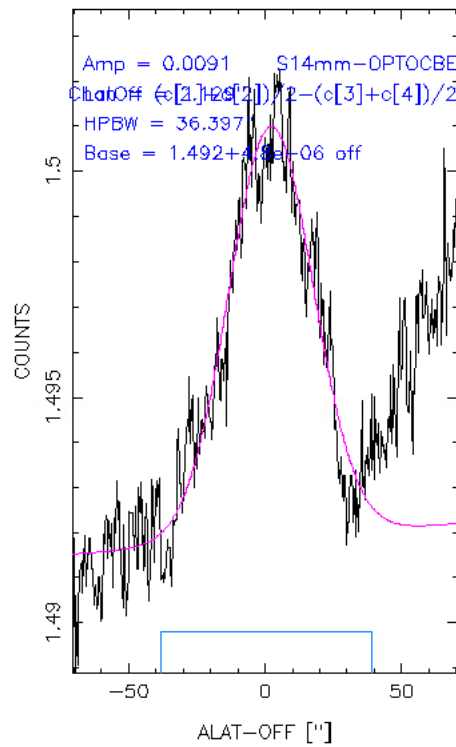
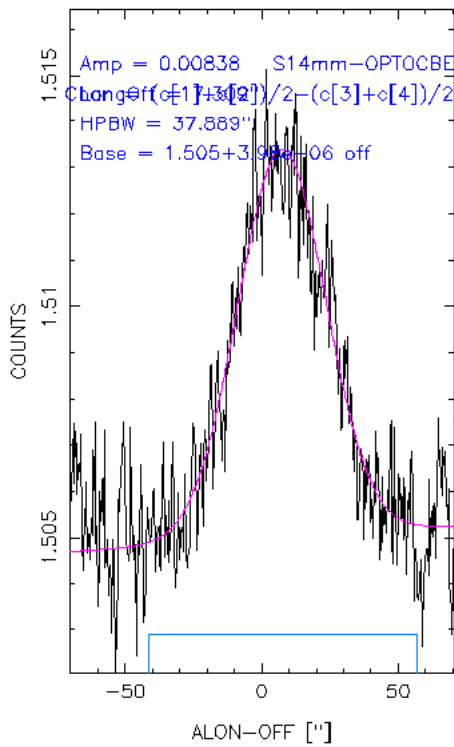


Figure 3.5: *Top:* Original (improved) scan using only the primary horn. *Bottom:* Same scan after subtracting the weather horn. This results in higher amplitudes and an overall better Gaussian behavior.

final flux density values. As described in the section above, the telescope measures the antenna/system temperature. In fact, this is not completely true. The signal is actually measured in counts and is then subsequently translated into temperature. To do this, the noise of the diode in the receiver needs to be known. Although the temperature of the noise diode T_{cal} changes with receiver and frequency, it is well known and tabulated on the [receiver page](#)⁵ of the telescope. Multiplying the counts with the corresponding T_{cal} results in the desired temperature

$$T_A [\text{K}] = T_{\text{cal}} [\text{K}] \cdot T_{\text{obs}} [\text{counts}]. \quad (3.5)$$

Taking a closer look at Fig. 3.4 and Fig. 3.5, it is evident that some of the scans are not centered around 0, but are rather shifted to the left or the right. This is due to the telescope deforming after moving so that it does not actually look at the exact position of the source, but is slightly off. The pointing offset is defined as the difference between the expected position of the source and the maximum of the telescope response. Calculating the corrected antenna temperature $T_{i,\text{poi}}$ is then achieved by using a Gaussian of the form

$$T_{i,\text{poi}} = T_i \cdot \exp \left(4 \ln 2 \cdot \left(\frac{\Delta p_j}{\theta} \right)^2 \right), \quad (3.6)$$

where i, j are the scanning direction indices with i : ELV, AZI and j : AZI, ELV, T_i is the antenna temperature for a scan over direction i , Δp_j is the pointing offset in the j direction and θ is the HPBW at the observing frequency. Note that the offset in the j direction is used to correct the measurement in the i direction and vice versa. Pointing offsets can be minimized by regularly doing cross-scans on bright nearby sources or doing an initial pointing scan before the actual measurement scan.

As was already explained, Earth's atmosphere leads to an attenuation of the observed signal. The dampening can be described by the factor $e^{\tau_{\text{atm}}}$, such that the opacity-corrected antenna temperature T_{opc} reads

$$T_{\text{opc}} = T_{\text{atm}} \cdot e^{\tau_{\text{atm}}}, \quad (3.7)$$

where τ_{atm} is the atmospheric opacity at the elevation ELV of the source. A useful factor to rewrite this equation is the air mass $AM = 1/\sin(ELV)$, which is a measure for the length of the path the signal has to travel in the atmosphere before arriving on Earth. With that, the atmospheric opacity can be expressed as

$$\tau_{\text{atm}} = \tau(ELV) = \tau_z \cdot AM = \tau_z \cdot (1/\sin(ELV)), \quad (3.8)$$

where τ_z is the zenith opacity. Overall, the system temperature can now be calculated via

$$\begin{aligned} T_{\text{sys}} &= T_0 + T_{\text{atm}} \cdot (1 - e^{-\tau_z \cdot AM}) \\ &\simeq T_0 + T_{\text{atm}} \cdot \tau_z \cdot AM. \end{aligned} \quad (3.9)$$

While T_{sys} is usually known and T_{atm} can be approximated to be the air temperature, T_0 can be derived by plotting the system temperature for an entire session and an individual frequency against the air mass and using a linear least-square-fit to determine the system temperature at zero air mass. Now, using Eq. 3.9, the zenith opacity τ_z can be calculated. To demonstrate the influence of the frequency on the opacity, Fig. 3.6 shows the zenith opacity plotted against time for an entire session at 19.25 GHz and 43.75 GHz. The higher frequency shows nearly double the opacity of the lower one. Especially at higher frequencies the opacity becomes important and contributes most to the error of the flux densities.

An alternative way of determining the opacity is presented by the water-vapor radiometer near the telescope that determines the opacity instantly by measuring the strength of the 22 GHz water-vapor line. While the latter is more straightforward, both ways are equally functional.

⁵https://eff100mwiki.mpifr-bonn.mpg.de/doku.php?id=information_for_astronomers:rx_list

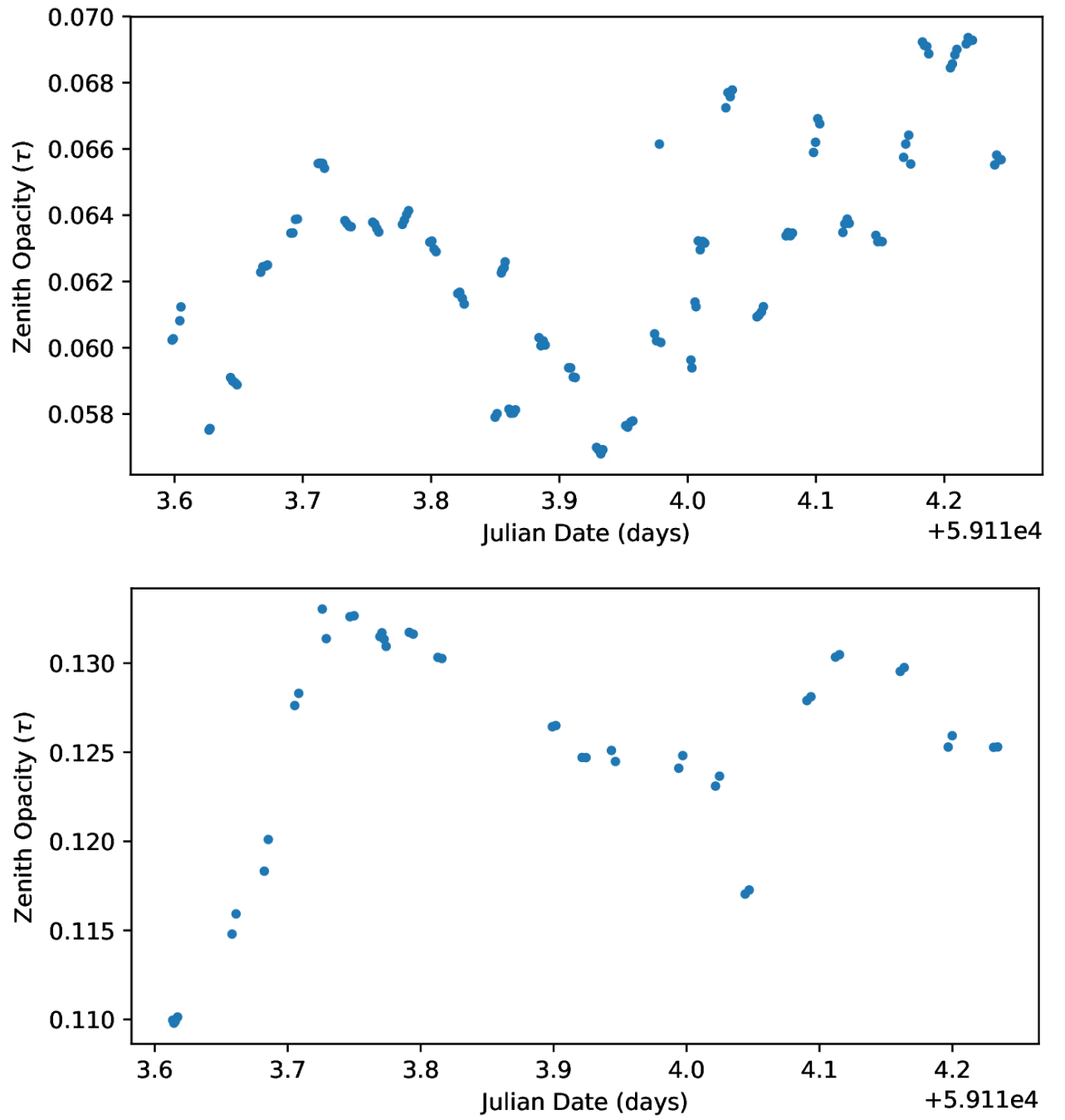


Figure 3.6: Exemplary zenith opacity τ for an observation session, plotted against time. *Top:* 19.25 GHz
Bottom: 43.75 GHz. Higher frequencies generally show a higher zenith opacity.

The last modification done to the data is the one to correct for elevation-dependent gain errors. Although the telescope always keeps its parabolic form when moving due to it being build using the principle of homology, small-scale deformations caused by gravity can still happen. Using a second-order polynomial function of the source ELV usually approximates the caused power loss well enough. The corrected antenna temperature then reads

$$T_{\text{gc}} = T \cdot G^{-1}, \quad (3.10)$$

where G is the gain curve for the used frequency, which can be expressed as

$$G = A_0 + A_1 \cdot ELV + A_2 \cdot ELV^2. \quad (3.11)$$

The parameters A_0 , A_1 and A_2 can also be taken from the corresponding receiver page of the telescope website.

To obtain the final flux densities, the antenna temperatures need to be converted into Jy. As it is difficult to calculate the aperture efficiency η_A a priori, and Eq. 3.2 and Eq. 3.3 only calculate the theoretically possible sensitivity, the actual sensitivity Γ is determined by comparing the measured flux densities of the aforementioned calibrators with their expected values and a „calibration factor“ can be derived. This calibration factor describes by which factor the observed values differ from the expected ones and is the inverse of the sensitivity $\Gamma_c = \Gamma^{-1}$. Consequently, multiplying this factor to the data results in the final calibrated flux densities

$$S [\text{Jy}] = \Gamma_c [\text{Jy/K}] \cdot T_A [\text{K}] = \frac{T_A [\text{K}]}{\Gamma [\text{K/Jy}]}. \quad (3.12)$$

Since the calibration factor can change over time, several calibrators are observed in each session. The calibration factor is then calculated as a mean value of all individual calibration factors and the calibration factor error is determined as the standard deviation of the individual factors. In principle, the calibration factors should all be the same, however, due to many, sometimes unknown factors, they differ from each other. The reasons include noise in the receiver, changes in the atmosphere and many more. Understanding the origin of the calibration factor error could probably fill another thesis.

In some rare cases, the calibration factors of different sources observed at different times throughout the session can vary tremendously, giving rise to huge uncertainties and wrong calibrations. Here, a linear interpolation between the different calibration factors would probably be best to correctly model its time evolution. However, such deviations in the calibration factors could also be explained by the variability of the calibrators themselves, as was already discovered for 3C 48 and 3C 147.

Overall, the final calibration includes

$$S = \frac{T_A \cdot e^{\tau z / \sin(ELV)}}{G \cdot \Gamma}. \quad (3.13)$$

To produce meaningful results, the flux densities need to have associated uncertainties as well. They arise through Gaussian error propagation from the correction steps above, although no error is added in the gain elevation step, as the gain curve is assumed to be free of errors. The biggest error is usually due to the uncertainty of the calibration factor, but also the atmospheric correction contributes noticeably. As for most sources and frequencies two scans were done, the flux density and error of each source can be calculated by using the weighted mean value and weighted error of both scans. When S_i is the flux density of a single scan, σ_i its uncertainty and n the number of total scans for a source, the weighted mean \bar{S} and the weighted standard error $\bar{\sigma}$ are defined as

$$\bar{S} = \sum_{i=1}^n \left(\frac{S_i}{\sigma_i^2} \right) / \sum_{i=1}^n \left(\frac{1}{\sigma_i^2} \right) \quad (3.14)$$

$$\bar{\sigma} = \sqrt{\left(\sum_{i=1}^n \sigma_i^{-2} \right)^{-1}}. \quad (3.15)$$

The formal error, especially for weaker sources, can sometimes be really small, which would not depict the real repeatability of the measurement. To counteract this, a second error is calculated from the standard deviation of the individual scans for a source. Now, the bigger of those two errors is assumed as the final error for a source's flux density. This is more of a conservative estimate and potentially overestimates the error. Additionally, a global absolute error could also possibly contribute to the measurement uncertainty. As the persons in charge of the telescope do not normally observe weak sources at these frequencies, there is no experience in this regard, but the continuation of the monitoring program could help in finding a potential error.

4 | Results

In this chapter the results for the data reduction of all sources in Table 2.1 are reported.

For the monitoring program, observations are conducted about once to twice per month. The concrete dates of the observations so far were the 25.08.2020, 21.09.2020, 18.10.2020, 12.11.2020 and 27.11.2020 as well as additional dates in December of 2020 and in the beginning of 2021. The original goal of this work was to present the first-light data of each source, and as such, the first epoch should be used. However, while reducing the data of the 25.08. epoch, a systematic offset between the 1.3 cm and 7 mm data was evident. Further investigations showed that even the scans of the bright calibrators did not yield satisfactory results, leading to the conclusion that the scans of the actual sources cannot be of satisfying quality either. This stands to reason, as the weather during the observation was very windy and rainy. Therefore, the first epoch will be ignored and the 21.09. epoch was chosen as the main epoch for this work. As not all sources were observed in this epoch, the data for the remaining ones were collected from the other observation sessions that were explicitly named above.

Table A.1 in the appendix holds all flux densities and their associated uncertainties for each source and each frequency that was not flagged and excluded during the data reduction. Where there are no entries for a certain frequency, they were either not observed or were excluded during the reduction. Sources with no entries at all were not detected during the observations.

As already mentioned, the emission of blazars in the radio band is mainly attributed to synchrotron radiation. Assuming the energy distribution of relativistic electrons to follow $N(E) dE \approx E^{-p} dE$, where p is the particle index, the resulting radio spectrum can be approximated by a power law

$$F_\nu \propto \nu^\alpha, \quad (4.1)$$

where $\alpha = (1 - p)/2$ is the spectral index (Rybicki & Lightman, 2008) and F_ν is the flux density at frequency ν . To compute the spectral index, the calculated flux densities at their corresponding frequency for each source were plotted in a $\log F_\nu - \log \nu$ diagram and a linear fit was used. All plots of the spectra are shown in Fig. A.1 in the appendix and the spectral indices as well as the mean flux densities (calculated according to Eq. 3.14) are reported in Table 4.1. Note that Table 4.1 shows the spectral indices of all sources that were detected (with the exception of 1428+4240 (1ES 1426+428), as here only two frequencies still showed results after the data reduction, making a fit not reasonable), however, in Fig. A.1 the fit is only drawn for sources with more than four frequencies.

To get a better overview of the data, two histograms, Fig. 4.1 and Fig. 4.2, are provided.

Figure 4.1 shows that most sources exhibit a mean flux density between 0.1 Jy to 1 Jy, with a few stronger and some weaker sources. Of all sources in the 0.1 Jy to 1 Jy range, most are actually weaker than 0.4 Jy. This confirms that the Effelsberg telescope is capable of detecting weaker sources than the OVRO or Metsähovi monitoring programs.

A representation of all spectral indices is displayed in Fig. 4.2. To be precise, only those sources with more than four surviving frequencies were considered in this plot, as the spectral shape of sources with

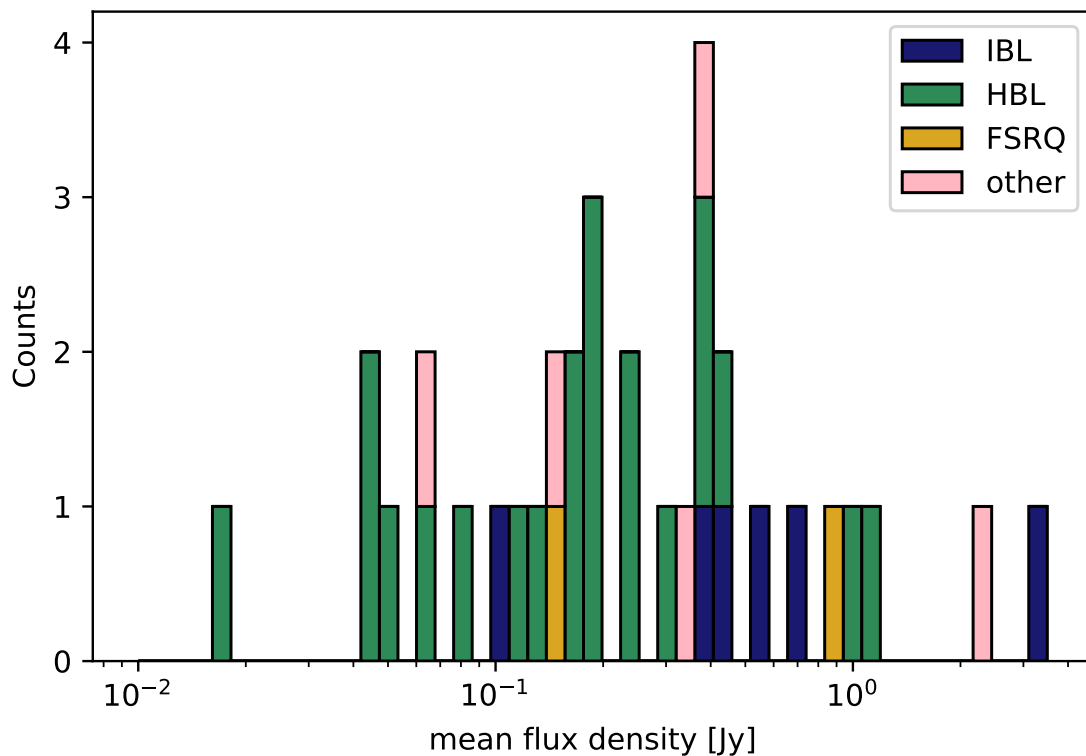


Figure 4.1: Histogram of the mean flux densities of all observed sources.

only four or less frequencies from the same receiver cannot safely be determined without potentially inscribing the fit to wrong values. Additionally, 0507+6737 (1ES 0502+675) was excluded from the plot as well, as it showed a highly unphysical, i.e., not approximately flat, spectral index of $\alpha \sim 3.6$. In future observations of this source, the 7 mm frequencies were never detected again, making a case against the validity of these measurements. This was the only case of such an unphysical spectral index within the sub-sample of sources with more than four frequencies left after data reduction. Overall, 24 sources have a „good“ spectral index, of which 13 are HBLs or extreme HBLs.

In a study of γ -ray selected blazars of the *Fermi* LAT Bright AGN Sample (LBAS), [Abdo et al. \(2010\)](#) assembled quasi-simultaneous SEDs of 48 LBAS blazars. For a frequency range between ~ 1 GHz and 8.4 GHz, they were able to calculate the radio spectral index for these sources and find an average of $\alpha_{\text{LBAS}} = -0.03$ with a standard deviation of $\sigma_{\text{LBAS}} = 0.23$, including both FSRQs and BL Lacs. Examining the sub-samples individually results in $\alpha_{\text{FSRQ}} = -0.002$, $\sigma_{\text{FSRQ}} = 0.23$ and $\alpha_{\text{BL Lac}} = -0.02$, $\sigma_{\text{BL Lac}} = 0.30$. Running a Kolmogorov-Smirnov (KS) test, which gives an estimate of how likely it is that two samples come from the same population, gives a probability of 43% that both samples come from the same parent population. They therefore conclude that the radio slope is quite flat ($\alpha \sim 0$) and that it is the same for all blazars.

To test if the spectral indices of the largest group in our sample, the HBLs, follow a normal distribution with parameters $\alpha = 0$, $\sigma = 1$, a KS test was performed. With a p -value of ~ 0.0035 , the null-hypothesis that their spectral indices are indeed normally distributed has to be rejected on a 2.9σ significance level, i.e., the probability that the sample was chosen from an intrinsically normally distributed population of blazars at random is only $\sim 0.36\%$.

In a next step it seems logical to test if the HBLs fit the BL Lac parameters ($\alpha = -0.02$, $\sigma = 0.30$)

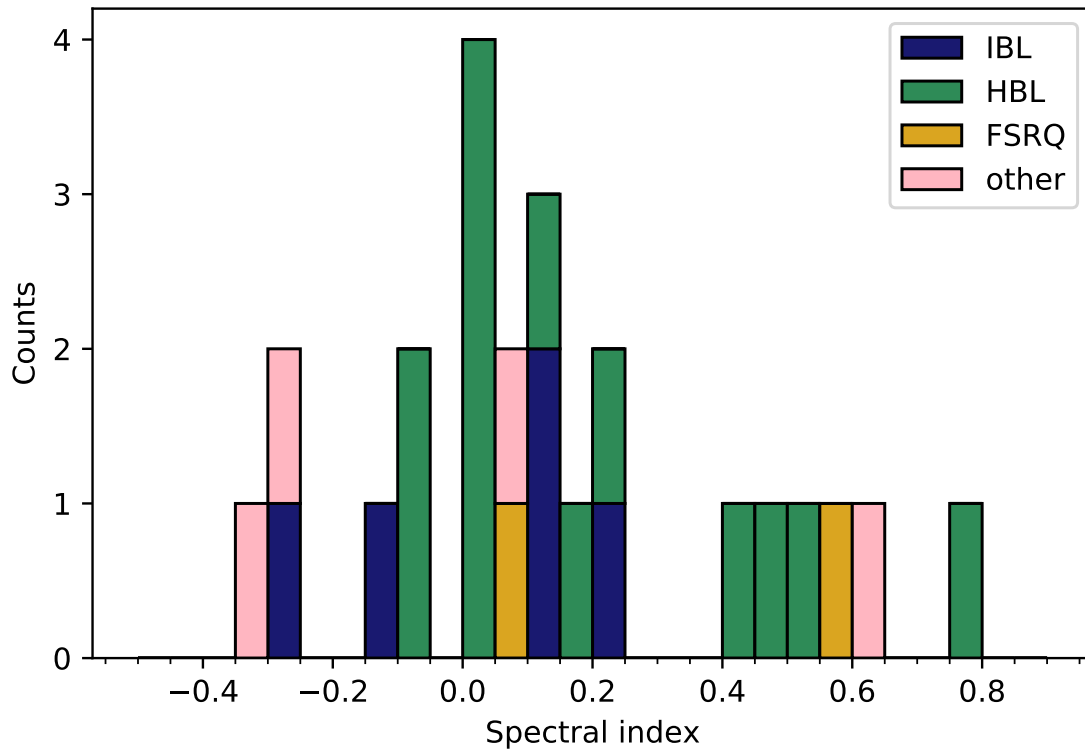


Figure 4.2: Histogram of the spectral indices of all observed sources that had data for more than four frequencies after the data reduction.

found by [Abdo et al. \(2010\)](#). However, this results in a p -value of < 0.01 , so the null-hypothesis that the spectral indices of HBLs follow the aforementioned „BL Lac parameters“ still has to be rejected on a 2.58σ significance level.

While FSRQs and LBLs are canonically known to have flat spectra, the HBLs studied show an increase in their brightness in the millimeter wavelength regime. This proves that HBLs are a special type of blazars.

Name (J2000)	Common name	Spectral index α	Mean flux density [Jy]	Date ^c
0035+5950	1ES 0033+595 ^b	-0.54 ± 0.53	0.0641 ± 0.0028	12.11
0112+2244	S2 0109+22	0.12 ± 0.15	0.689 ± 0.022	21.09
0214+5144	TXS 0210+515	0.55 ± 0.27	0.1370 ± 0.0049	12.11
0222+4302	3C 66A	-0.07 ± 0.12	1.074 ± 0.020	21.09
0232+2017	1ES 0229+200 ^b	1.1 ± 1.0	0.0441 ± 0.0036	12.11
0303-2407	PKS 0301-243 ^b	0.44 ± 0.41	0.182 ± 0.060	21.09
0316+4119	IC 310	0.62 ± 0.24	0.1537 ± 0.0054	21.09
0416+0105	1ES 0414+009 ^b	3.7 ± 3.2	0.0470 ± 0.0037	21.09
0507+6737	1ES 0502+675 ^b	3.63 ± 0.45	0.0181 ± 0.0018	12.11
0509+0541	TXS 0506+056	0.09 ± 0.13	2.263 ± 0.052	21.09
0521+2112	RGB J0521+212	0.10 ± 0.12	0.3668 ± 0.0068	21.09
0650+2502	1ES 0647+250 ^a	–	–	19.12
0658+0637	4FGL J0658.6+0636 ^a	–	–	27.11
0955+3551	3HSP J095507.9+35510 ^a	–	–	21.09
1015+4926	1ES 1011+496	0.16 ± 0.17	0.2456 ± 0.0046	21.09
1104+3812	Mrk 421	0.00 ± 0.19	0.371 ± 0.013	21.09
1136+7009	Mrk 180	0.00 ± 0.26	0.1665 ± 0.0049	21.09
1145+1936	3C 264	-0.29 ± 0.17	0.3222 ± 0.0082	21.09
1217+3007	ON 325	0.03 ± 0.16	0.363 ± 0.012	21.09
1221+2813	W Comae	-0.25 ± 0.14	0.544 ± 0.010	21.09
1221+3010	1ES 1218+304 ^b	-0.02 ± 0.70	0.0806 ± 0.0050	27.11
1230+2518	ON 246	-0.14 ± 0.14	0.4103 ± 0.0079	21.09
1259+0136	PKS 1256+018 ^b	-0.6 ± 1.5	0.0605 ± 0.0046	27.11
1422+3223	OQ 334	0.07 ± 0.18	0.838 ± 0.023	12.11
1427+2348	OQ 240	0.11 ± 0.12	0.4428 ± 0.0085	21.09
1428+4240	1ES 1426+428 ^d	–	0.0532 ± 0.0070	21.09
1443+2501	PKS 1441+25	0.585 ± 0.071	0.1487 ± 0.0025	18.10
1518-2731	TXS 1515-273 ^a	–	–	24.10
1555+1111	PG 1553+113	0.42 ± 0.15	0.3045 ± 0.0062	21.09
1653+3945	Mrk 501	-0.06 ± 0.14	1.010 ± 0.023	21.09
1728+5013	I Zw 187	0.75 ± 0.15	0.1183 ± 0.0031	21.09
1743+1935	1ES 1741+196	0.49 ± 0.21	0.1764 ± 0.0068	21.09
1813+3144	B2 1811+31 ^b	-0.37 ± 0.86	0.1069 ± 0.0054	18.10
1959+6508	1ES 1959+650	0.24 ± 0.26	0.2358 ± 0.0069	21.09
2018+3851	TXS 2016+386	-0.32 ± 0.30	0.383 ± 0.016	27.11
2158-3013	PKS 2155-304 ^b	-2.01 ± 0.46	0.198 ± 0.012	27.11
2202+4216	BL Lac	0.23 ± 0.14	3.273 ± 0.060	21.09
2347+5142	1ES 2344+514	0.02 ± 0.27	0.1680 ± 0.0091	21.09

Table 4.1: Table of sources considered in this work, along with their spectral index α and their mean flux density. ^a Sources were observed but did not yield any results, ^b Sources were not included in the spectral index histogram, as no more than four frequencies each still showed results after the data reduction (1ES 0502+675 was excluded as its spectral index is highly unphysical), ^c The date of the observation the data were taken from, ^d Source only had two frequencies left after data reduction, making a fit not reasonable.

This thesis represents a first look at the sources included in the long term monitoring program of TeV blazars. The results prove that it is possible to observe weak sources at high frequencies for good weather conditions using the Effelsberg 100 m telescope. However, there are still problems that need to be dealt with that would exceed the means of this thesis. The variability of the calibration sources 3C 48 and 3C 147 has to be checked by further observations and the error calculation of the final flux densities needs to be refined, as there is no physical argument for the way it is currently done other than not to underestimate the error. A possible alternative was already used by [Angelakis et al. \(2009\)](#) and [Angelakis et al. \(2019\)](#), who used the information of the entire lightcurve, divided into a flux-dependent and flux-independent term. They computed the scatter of the flux densities of each calibrator to determine the repeatability of a measurement and used this value to calculate the errors. Furthermore, efforts to understand a potential absolute error need to be made. For this, the flux densities of weak calibration sources will be compared to those of strong calibrators. Future works will not only try to solve these problems, but also present light curves of all sources and further analyze their properties.

As a matter of fact, this monitoring program includes several sources that are regularly observed by other programs in different energy bands. The FACT collaboration¹ regularly observes sources such as Mrk 421 and Mrk 501 at TeV energies. The Effelsberg data can then be used to study the correlation between the radio and TeV variability and to derive time lags during flares.

Next to others, the same previous sources are also included in the monitoring program of the VERITAS collaboration² observing at GeV to TeV energies.

Furthermore, other sources of this sample are also regularly observed by the H.E.S.S.³ and the MAGIC⁴ collaborations who are also sensitive to radiation in the GeV to TeV range. As it is the dawn of the new Cherenkov telescope array⁵ (CTA) era, which will be sensitive to even higher energies (~ 300 TeV), the understanding of TeV blazars achieved by this project can help in understanding these poorly studied sources.

By observing sources at the same time as other telescopes, simultaneous SEDs can be constructed. The radio data obtained here will also find ample use in general multiwavelength SED studies of AGN.

Moreover, eight extreme blazars will be observed by the Global mm-VLBI Array (GMVA)⁶ to image parsec scale structures and help in solving the Doppler crisis. The single dish data are highly important to connect and interpret these observations.

As was already done, the monitoring program can also contribute in finding counterparts to IceCube neutrinos. Detecting such sources could potentially confirm their HBL nature.

¹<https://www.isdc.unige.ch/fact/>

²<https://veritas.sao.arizona.edu/>

³<https://www.mpi-hd.mpg.de/hfm/HESS/>

⁴<https://magic.mpp.mpg.de/>

⁵<https://www.cta-observatory.org/>

⁶<https://www3.mpifr-bonn.mpg.de/div/vlbi/globalmm/>

Bibliography

- Abdo A., et al., 2010, *The Astrophysical Journal*, 716, 30
- Abdo A. A., et al., 2011, *The Astrophysical Journal*, 736, 131
- Albert J., et al., 2007, *The Astrophysical Journal*, 669, 862
- Angelakis E., et al., 2009, *Astronomy & Astrophysics*, 501, 801
- Angelakis E., et al., 2019, *Astronomy & Astrophysics*, 626, A60
- Antonucci R., 1993, *Annual review of astronomy and astrophysics*, 31, 473
- Bach U., Kraus A., Fürst E., Polatidis A., 2007, First report about the commissioning of the new Effelsberg sub-reflector. Effelsberg memo series
- Beckmann V., Shradler C. R., 2012, *Active Galactic Nuclei*. Wiley
- Biteau J., et al., 2020, *Nature Astronomy*, 4, 124–131
- Donato D., Ghisellini G., Tagliaferri G., Fossati G., 2001, *Astronomy & Astrophysics*, 375, 739
- Fossati G. a., Maraschi L., Celotti A., Comastri A., Ghisellini G., 1998, *Monthly Notices of the Royal Astronomical Society*, 299, 433
- Georganopoulos M., Kazanas D., 2003, *The Astrophysical Journal Letters*, 594, L27
- Ghisellini G., Celotti A., Fossati G., Maraschi L., Comastri A., 1998, *Monthly Notices of the Royal Astronomical Society*, 301, 451
- Ghisellini G., Tavecchio F., Chiaberge M., 2005, *Astronomy & Astrophysics*, 432, 401
- Ghisellini G., Righi C., Costamante L., Tavecchio F., 2017, *Monthly Notices of the Royal Astronomical Society*, 469, 255
- Giommi P., et al., 2012, *Monthly Notices of the Royal Astronomical Society*, 420, 2899
- Hönig S. F., 2019, *The Astrophysical Journal*, 884, 171
- Kellermann K., Sramek R., Schmidt M., Shaffer D., Green R., 1989, *The Astronomical Journal*, 98, 1195
- Lindfors E., et al., 2016, *Astronomy & Astrophysics*, 593, A98
- Lyutikov M., Lister M., 2010, *The Astrophysical Journal*, 722, 197
- Mannheim K., 1993, *Astronomy and Astrophysics*, 269, 67

- Ott M., et al., 1994, *Astronomy and Astrophysics*, 284, 331
- Padovani P., Giommi P., 1994, arXiv preprint astro-ph/9412073
- Padovani P., et al., 2017, *The Astronomy and Astrophysics Review*, 25, 2
- Padovani P., et al., 2018, *Monthly Notices of the Royal Astronomical Society*, 480, 192
- Pardo J. R., Cernicharo J., Serabyn E., 2001, *IEEE Transactions on antennas and propagation*, 49, 1683
- Piner B. G., Edwards P. G., 2015, in *Proceedings of the Fourteenth Marcel Grossmann Meeting On Recent Developments in Theoretical and Experimental General Relativity, Astrophysics, and Relativistic Field Theories*, Rome, Italy. pp 12–18
- Piner B. G., Edwards P. G., 2018, *The Astrophysical Journal*, 853, 68
- Ros E., et al., 2020, *Astronomy & Astrophysics*, 633, L1
- Ruze J., 1966, *Proceedings of the IEEE*, 54, 633
- Rybicki G. B., Lightman A. P., 2008, *Radiative processes in astrophysics*. John Wiley & Sons
- Sikora M., Madejski G., Moderski R., Poutanen J., 1997, *The Astrophysical Journal*, 484, 108
- Urry C. M., Padovani P., 1995, *Publications of the Astronomical Society of the Pacific*, 107, 803
- Vollmer B., et al., 2018, *Astronomy & Astrophysics*, 615, A164
- Woo J.-H., Urry C. M., 2002, *The Astrophysical Journal*, 579, 530

Acknowledgments

First and foremost I would like to thank Prof. Matthias Kadler for the opportunity to work on this brand new and exciting project. Next to this thesis, he invited me to work as a student assistant on the monitoring program, allowing me to gain much needed experience in working with the telescope, which did not only help with this thesis, but will certainly benefit me in future projects.

I am much obliged to Dr. Uwe Bach, who gave me an introduction to observing with the Effelsberg telescope and the data reduction procedure. He also gave me a tour of the entire telescope, including the very top of it as well as the inside of the dish. This is something not many people have done and I will keep these impressions for a very long time. When I had questions or problems regarding the observations, the calibration or the data reduction, he and Dr. Alex Kraus always helped in answering and fixing them.

I truly appreciate Andrea Gokus and Florian Eppel, who were there with me in Effelsberg when we pulled an all-nighter to do our first observation. They were also introduced to the observing and data reduction process and have been working together with me on the monitoring program ever since. Florian Rösch and Jonas Sinapius were later introduced into the program and now play an essential part in the observation-team as well. Without all of them, the observations for this thesis could not have been conducted. Also, Andrea, thank you for the help with the python scripts.

Even though I did not necessarily need this knowledge for my thesis, I want to thank Paul Ray Burd for introducing me to VLBI and Difmap. As the work on the monitoring program will be complemented by VLBI observations, an understanding of the basic concepts will for sure come in handy in the future.

Although I have not been able to meet everyone in the group of Matthias Kadler in person due to the pandemic, I always felt welcomed in the group meeting and other gatherings. Thank you for that.

Finally, I want to thank my parents, who always supported me in my studies and believed my decisions.

Based on observations with the 100-m telescope of the MPIfR (Max-Planck-Institut für Radioastronomie) at Effelsberg.

Declaration of authorship

I, Jonas Heßdörfer, declare that this thesis titled, 'Flux density measurements of TeV blazars with the Effelsberg 100 m telescope' and the work presented in it are my own. I confirm that:

- This work was done wholly or mainly while in candidature for a research degree at this University.
- Where any part of this thesis has previously been submitted for a degree or any other qualification at this University or any other institution, this has been clearly stated.
- Where I have consulted the published work of others, this is always clearly attributed.
- Where I have quoted from the work of others, the source is always given. With the exception of such quotations, this thesis is entirely my own work.
- I have acknowledged all main sources of help.

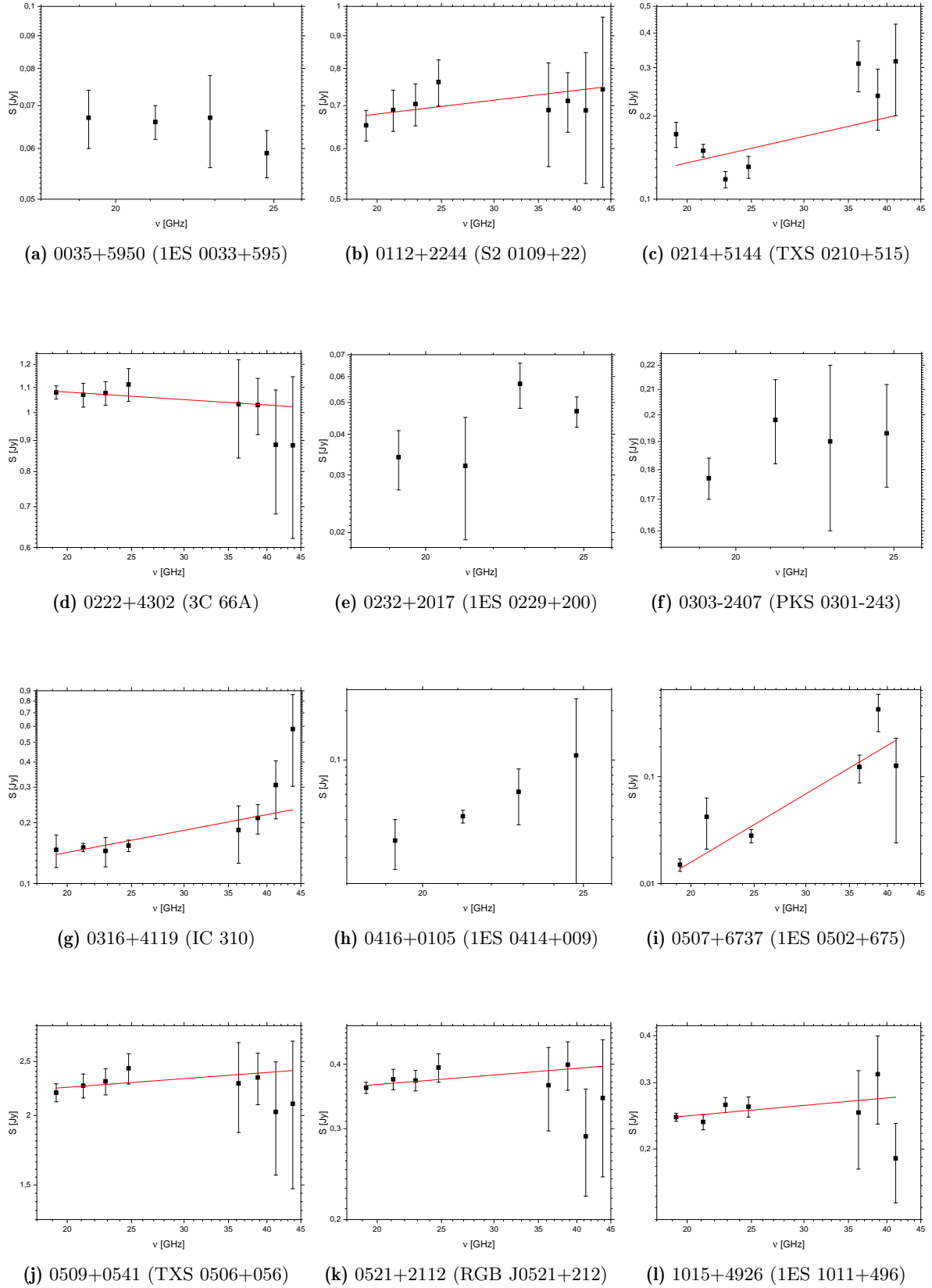
Signed: _____

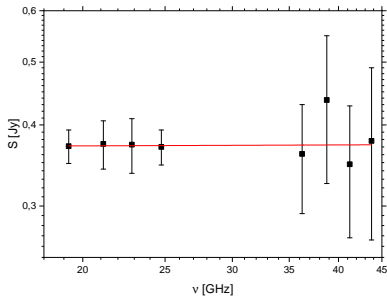
Date: _____

Appendices

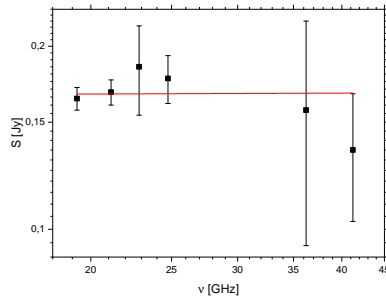
A | Spectra and data table

Figure A.1: Plots of the spectra of all observed sources. Where there were more than four frequencies left after the data reduction, a fit for the spectral index is also shown (red). See Table 4.1 for the date of observation for each source.

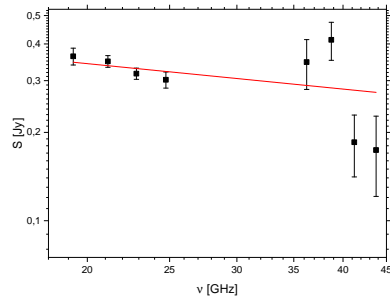




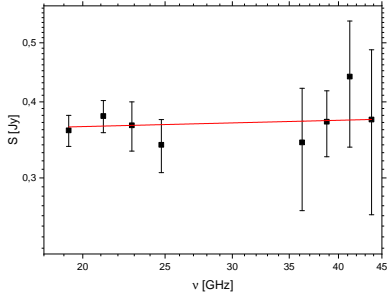
(m) 1104+3812 (Mrk 421)



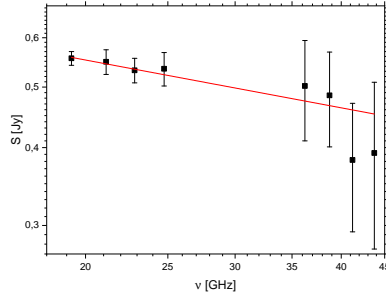
(n) 1136+7009 (Mrk 180)



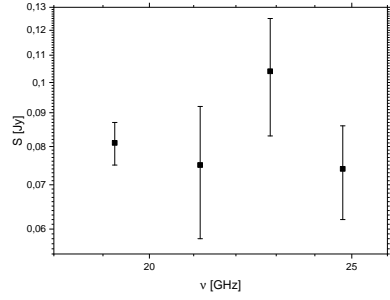
(o) 1145+1936 (3C 264)



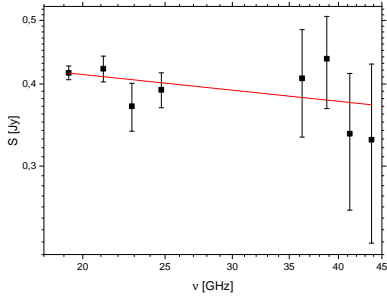
(p) 1217+3007 (ON 325)



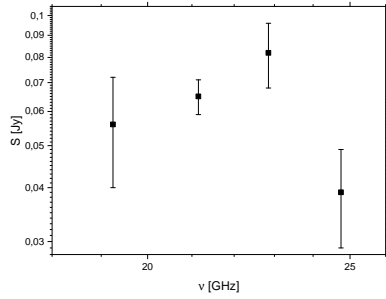
(q) 1221+2813 (W Comae)



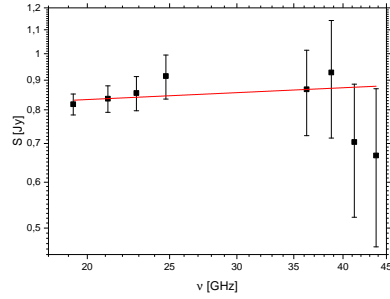
(r) 1221+3010 (1ES 1218+304)



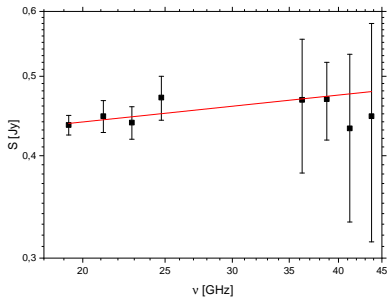
(s) 1230+2518 (ON 246)



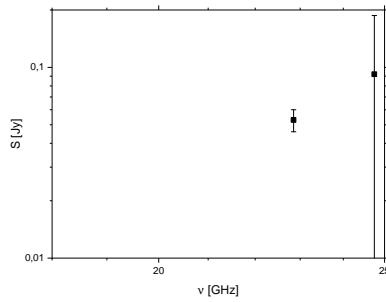
(t) 1259+0136 (PKS 1256+018)



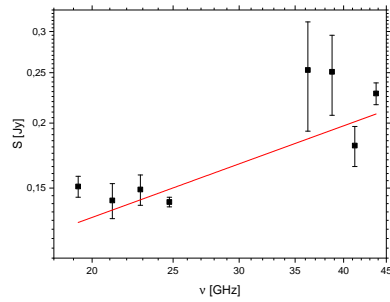
(u) 1422+3223 (OQ 334)



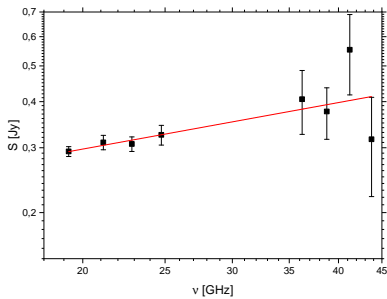
(v) 1427+2348 (OQ 240)



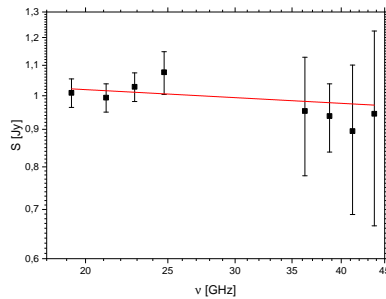
(w) 1428+4240 (1ES 1426+428)



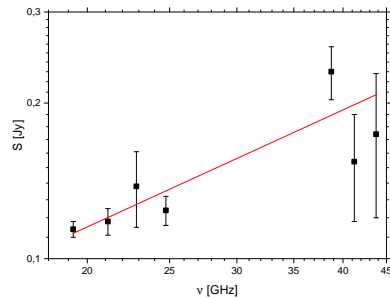
(x) 1443+2501 (PKS 1441+25)



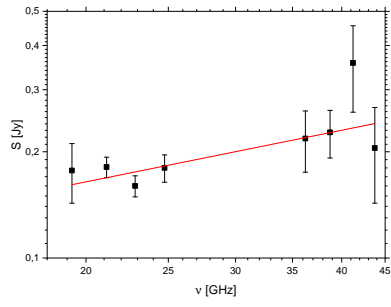
(y) 1555+1111 (PG 1553+113)



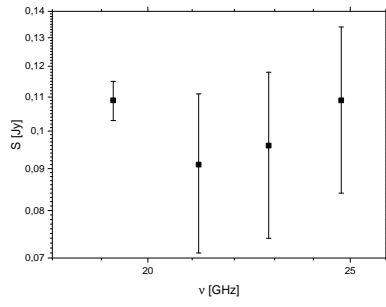
(z) 1653+3945 (Mrk 501)



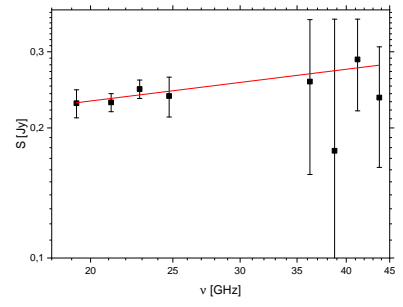
(aa) 1728+5013 (I Zw 187)



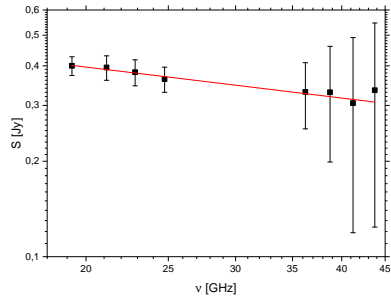
(ab) 1743+1935 (1ES 1741+196)



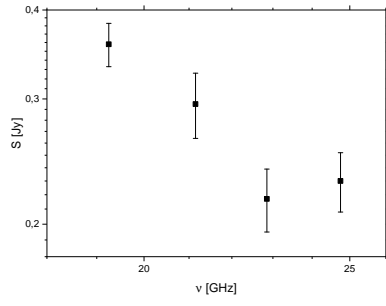
(ac) 1813+3144 (B2 1811+31)



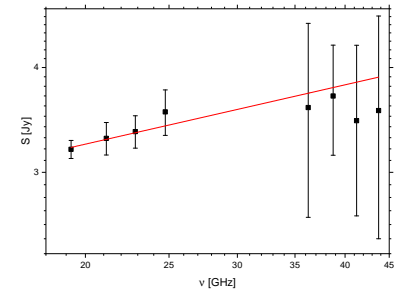
(ad) 1959+6508 (1ES 1959+650)



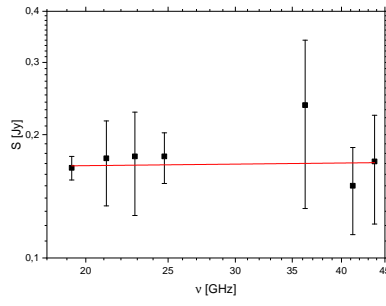
(ae) 2018+3851 (TXS 2016+386)



(af) 2158-3013 (PKS 2155-304)



(ag) 2202+4216 (BL Lac)



(ah) 2347+5142 (1ES 2344+514)

Table A.1: Flux densities at the corresponding frequencies for all sources.

Name (J2000)	Common name	Epoch	Frequency [GHz]	Flux density [Jy]
0035+5950	1ES 0033+595	12.11	19.25	0.067 ± 0.007
			21.15	0.066 ± 0.004
			22.85	0.067 ± 0.011
			24.75	0.059 ± 0.005
0112+2244	S2 0109+22	21.09	19.25	0.652 ± 0.036
			21.15	0.689 ± 0.051
			22.85	0.704 ± 0.053
			24.75	0.762 ± 0.063
			36.25	0.689 ± 0.127
			38.75	0.712 ± 0.076
			41.25	0.688 ± 0.159
0214+5144	TXS 0210+515	12.11	19.25	0.172 ± 0.018
			21.15	0.150 ± 0.008
			22.85	0.118 ± 0.008
			24.75	0.131 ± 0.012
			36.25	0.310 ± 0.065
			38.75	0.237 ± 0.059
			41.25	0.316 ± 0.115
0222+4302	3C 66A	21.09	19.25	1.079 ± 0.027
			21.15	1.069 ± 0.048
			22.85	1.076 ± 0.048
			24.75	1.112 ± 0.069
			36.25	1.032 ± 0.190
			38.75	1.029 ± 0.109
			41.25	0.885 ± 0.204
0232+2017	1ES 0229+200	12.11	19.25	0.034 ± 0.007
			21.15	0.032 ± 0.013
			22.85	0.057 ± 0.009
			24.75	0.047 ± 0.005
0303-2407	PKS 0301-243	21.09	19.25	0.177 ± 0.007
			21.15	0.198 ± 0.016
			22.85	0.190 ± 0.031
			24.75	0.193 ± 0.019

Name (J2000)	Common name	Epoch	Frequency [GHz]	Flux density [Jy]
0316+4119	IC 310	21.09	19.25	0.147 ± 0.027
			21.15	0.151 ± 0.007
			22.85	0.145 ± 0.024
			24.75	0.154 ± 0.010
			36.25	0.184 ± 0.058
			38.75	0.211 ± 0.035
			41.25	0.307 ± 0.098
			43.75	0.582 ± 0.279
0416+0105	1ES 0414+009	21.09	19.25	0.035 ± 0.011
			21.15	0.048 ± 0.004
			22.85	0.066 ± 0.023
			24.75	0.106 ± 0.116
0507+6737	1ES 0502+675	12.11	19.25	0.015 ± 0.002
			21.15	0.042 ± 0.021
			24.75	0.028 ± 0.004
			36.25	0.123 ± 0.036
			38.75	0.425 ± 0.162
			41.25	0.126 ± 0.102
0509+0541	TXS 0506+056	21.09	19.25	2.198 ± 0.082
			21.15	2.262 ± 0.112
			22.85	2.303 ± 0.125
			24.75	2.430 ± 0.152
			36.25	2.284 ± 0.420
			38.75	2.340 ± 0.249
			41.25	2.030 ± 0.467
			43.75	2.099 ± 0.622
0521+2112	RGB J0521+212	21.09	19.25	0.360 ± 0.009
			21.15	0.374 ± 0.017
			22.85	0.372 ± 0.017
			24.75	0.394 ± 0.025
			36.25	0.364 ± 0.067
			38.75	0.399 ± 0.043
			41.25	0.290 ± 0.068
			43.75	0.344 ± 0.102
0650+2502	1ES 0647+250	19.12		
0658+0637	4FGLJ0658.6+0636	27.11		
0955+3551	3HSP J095507.9+35510	21.09		

Name (J2000)	Common name	Epoch	Frequency [GHz]	Flux density [Jy]
1015+4926	1ES 1011+496	21.09	19.25	0.243 ± 0.006
			21.15	0.236 ± 0.011
			22.85	0.262 ± 0.012
			24.75	0.259 ± 0.016
			36.25	0.250 ± 0.073
			38.75	0.316 ± 0.083
			41.25	0.189 ± 0.045
1104+3812	Mrk 421	21.09	19.25	0.371 ± 0.022
			21.15	0.374 ± 0.032
			22.85	0.373 ± 0.036
			24.75	0.370 ± 0.023
			36.25	0.361 ± 0.069
			38.75	0.437 ± 0.112
			41.25	0.348 ± 0.080
1136+7009	Mrk 180	21.09	19.25	0.164 ± 0.007
			21.15	0.168 ± 0.008
			22.85	0.185 ± 0.031
			24.75	0.177 ± 0.016
			36.25	0.157 ± 0.063
			41.25	0.135 ± 0.032
			1145+1936	3C 264
21.15	0.349 ± 0.016			
22.85	0.317 ± 0.014			
24.75	0.302 ± 0.019			
36.25	0.347 ± 0.067			
38.75	0.413 ± 0.061			
41.25	0.185 ± 0.044			
1217+3007	ON 325	21.09	19.25	0.359 ± 0.021
			21.15	0.373 ± 0.023
			22.85	0.366 ± 0.034
			24.75	0.340 ± 0.034
			36.25	0.343 ± 0.078
			38.75	0.371 ± 0.046
			41.25	0.440 ± 0.103
43.75	0.374 ± 0.113			

Name (J2000)	Common name	Epoch	Frequency [GHz]	Flux density [Jy]
1221+2813	W Comae	21.09	19.25	0.556 ± 0.014
			21.15	0.549 ± 0.025
			22.85	0.532 ± 0.024
			24.75	0.535 ± 0.033
			36.25	0.502 ± 0.092
			38.75	0.485 ± 0.084
			41.25	0.382 ± 0.089
			43.75	0.392 ± 0.117
1221+3010	1ES 1218+304	27.11	19.25	0.081 ± 0.006
			21.15	0.075 ± 0.017
			22.85	0.104 ± 0.021
			24.75	0.074 ± 0.012
1230+2518	ON 246	21.09	19.25	0.416 ± 0.010
			21.15	0.422 ± 0.019
			22.85	0.370 ± 0.031
			24.75	0.392 ± 0.024
			36.25	0.408 ± 0.076
			38.75	0.437 ± 0.070
			41.25	0.336 ± 0.079
			43.75	0.329 ± 0.100
1259+0136	PKS 1256+018	27.11	19.25	0.056 ± 0.016
			21.15	0.065 ± 0.006
			22.85	0.082 ± 0.014
			24.75	0.039 ± 0.010
1422+3223	OQ 334	12.11	19.25	0.818 ± 0.034
			21.15	0.847 ± 0.044
			22.85	0.855 ± 0.058
			24.75	0.915 ± 0.080
			36.25	0.868 ± 0.146
			38.75	0.928 ± 0.213
			41.25	0.704 ± 0.182
			43.75	0.667 ± 0.203
1427+2348	OQ 240	21.09	19.25	0.436 ± 0.012
			21.15	0.447 ± 0.020
			22.85	0.439 ± 0.020
			24.75	0.471 ± 0.029
			36.25	0.468 ± 0.087
			38.75	0.469 ± 0.051
			41.25	0.432 ± 0.100
			43.75	0.447 ± 0.133

Name (J2000)	Common name	Epoch	Frequency [GHz]	Flux density [Jy]
1428+4240	1ES 1426+428	21.09	22.85	0.053 ± 0.007
			24.75	0.092 ± 0.095
1443+2501	PKS 1441+25	18.10	19.25	0.151 ± 0.007
			21.15	0.142 ± 0.011
			22.85	0.149 ± 0.010
			24.75	0.141 ± 0.003
			36.25	0.253 ± 0.060
			38.75	0.251 ± 0.044
			41.25	0.181 ± 0.016
			43.75	0.228 ± 0.011
1518-2731	TXS 1515-273	24.10		
1555+1111	PG 1553+113	21.09	19.25	0.293 ± 0.009
			21.15	0.310 ± 0.014
			22.85	0.307 ± 0.014
			24.75	0.325 ± 0.020
			36.25	0.406 ± 0.080
			38.75	0.376 ± 0.060
			41.25	0.553 ± 0.136
			43.75	0.316 ± 0.095
1653+3945	Mrk 501	21.09	19.25	1.009 ± 0.045
			21.15	0.994 ± 0.044
			22.85	1.028 ± 0.046
			24.75	1.076 ± 0.072
			36.25	0.953 ± 0.175
			38.75	0.938 ± 0.100
			41.25	0.895 ± 0.206
			43.75	0.945 ± 0.280
1728+5013	I Zw 187	21.09	19.25	0.114 ± 0.004
			21.15	0.118 ± 0.007
			22.85	0.138 ± 0.023
			24.75	0.124 ± 0.008
			38.75	0.230 ± 0.027
			41.25	0.154 ± 0.036
			43.75	0.174 ± 0.054

Name (J2000)	Common name	Epoch	Frequency [GHz]	Flux density [Jy]
1743+1935	1ES 1741+196	21.09	19.25	0.177 ± 0.034
			21.15	0.181 ± 0.012
			22.85	0.160 ± 0.011
			24.75	0.180 ± 0.016
			36.25	0.218 ± 0.043
			38.75	0.227 ± 0.035
			41.25	0.357 ± 0.098
			43.75	0.205 ± 0.062
1813+3144	B2 1811+31	18.10	19.25	0.109 ± 0.006
			21.15	0.091 ± 0.020
			22.85	0.096 ± 0.022
			24.75	0.109 ± 0.025
1959+6508	1ES 1959+650	21.09	19.25	0.228 ± 0.017
			21.15	0.229 ± 0.011
			22.85	0.246 ± 0.012
			24.75	0.237 ± 0.025
			36.25	0.256 ± 0.100
			38.75	0.177 ± 0.180
			41.25	0.288 ± 0.069
			43.75	0.235 ± 0.073
2018+3851	TXS 2016+386	27.11	19.25	0.400 ± 0.027
			21.15	0.395 ± 0.035
			22.85	0.382 ± 0.036
			24.75	0.363 ± 0.033
			36.25	0.331 ± 0.078
			38.75	0.330 ± 0.131
			41.25	0.305 ± 0.186
			43.75	0.335 ± 0.211
2158-3013	PKS 2155-304	27.11	19.25	0.358 ± 0.025
			21.15	0.295 ± 0.031
			22.85	0.217 ± 0.022
			24.75	0.230 ± 0.022

Name (J2000)	Common name	Epoch	Frequency [GHz]	Flux density [Jy]
2202+4216	BL Lac	21.09	19.25	3.196 ± 0.079
			21.15	3.293 ± 0.147
			22.85	3.355 ± 0.149
			24.75	3.541 ± 0.221
			36.25	3.584 ± 0.932
			38.75	3.699 ± 0.555
			41.25	3.457 ± 0.795
			43.75	3.554 ± 1.054
2347+5142	1ES 2344+514	21.09	19.25	0.166 ± 0.011
			21.15	0.175 ± 0.041
			22.85	0.177 ± 0.050
			24.75	0.177 ± 0.025
			36.25	0.236 ± 0.104
			41.25	0.150 ± 0.036
			43.75	0.172 ± 0.051

B | A guide to reducing pointed flux measurements obtained by the Effelsberg 100 m telescope

```
# This guide describes the process of reducing and analyzing
# cross-scan data for pointed flux density measurements
# obtained by the Effelsberg 100 m telescope.
#
# Phrases written in red need to be adapted to the
# current step in the analysis accordingly.
#
# Phrases in green are commands that are called in the command line.
#
# The data reduction is performed using the Observer-PCs
# in the MPIfR network.
# A connection to those machines is achieved
# by logging into a MPIfR account via ssh tunneling.
#
# The working folder for the 81-20 project is /home/obs2/81-20/
# Here, create a date-folder of the form YYYY_MM_DD for
# the date of the observation to be analyzed.
# All further analysis will now be done in this folder.
> cd /home/obs2/81-20
> mkdir 202X_XX_XX
> cd 202X_XX_XX

# First, open the Obslogger, find the required data by inputting
# a start and end time for the observation as well as
# the project code (81-20) and export the log as a text file.
> obslog

# The following part needs to be carried out
# for each individual frequency.
```

Obs logger															
Scan	FEBE	Baseband	First sub	Last sub	Time (UTC)	Time (LST)	Date	Object	Observer	Project ID	Scan type	Scan mode	Obs type	Ctrl buttons (Az/El/Foc/Sur)	Longitude (HH:MM:SS)
236	2584	S7mm-OPTOCBE	1	4	16:33:57	15:19 to 15:21	Aug 25, 2020	3C345	BACH/KISKY	81-20	POINT	OTF	ON	0 / 0 / 0 / 0	16:41:1
237	2584	S7mm-OPTOCBE	2	1	16:33:57	15:19 to 15:21	Aug 25, 2020	3C345	BACH/KISKY	81-20	POINT	OTF	ON	0 / 0 / 0 / 0	16:41:1
238	2583	S14mm-OPTOCBE	1	4	16:30:58	15:16 to 15:18	Aug 25, 2020	3C345	BACH/KISKY	81-20	POINT	OTF	ON	0 / 0 / 0 / 0	16:41:1
239	2583	S14mm-OPTOCBE	2	1	16:30:58	15:16 to 15:18	Aug 25, 2020	3C345	BACH/KISKY	81-20	POINT	OTF	ON	0 / 0 / 0 / 0	16:41:1
240	2583	S14mm-OPTOCBE	3	1	16:30:58	15:16 to 15:18	Aug 25, 2020	3C345	BACH/KISKY	81-20	POINT	OTF	ON	0 / 0 / 0 / 0	16:41:1
241	2583	S14mm-OPTOCBE	4	1	16:30:58	15:16 to 15:18	Aug 25, 2020	3C345	BACH/KISKY	81-20	POINT	OTF	ON	0 / 0 / 0 / 0	16:41:1
242	2582	S14mm-OPTOCBE	1	2	16:28:40	15:13 to 15:14	Aug 25, 2020	3C345	BACH/KISKY	81-20	FOCUS	SAMPLE	ON	0 / 0 / 0 / 0	16:41:1
243	2582	S14mm-OPTOCBE	2	1	16:28:40	15:13 to 15:14	Aug 25, 2020	3C345	BACH/KISKY	81-20	FOCUS	SAMPLE	ON	0 / 0 / 0 / 0	16:41:1
244	2582	S14mm-OPTOCBE	3	1	16:28:40	15:13 to 15:14	Aug 25, 2020	3C345	BACH/KISKY	81-20	FOCUS	SAMPLE	ON	0 / 0 / 0 / 0	16:41:1
245	2582	S14mm-OPTOCBE	4	1	16:28:40	15:13 to 15:14	Aug 25, 2020	3C345	BACH/KISKY	81-20	FOCUS	SAMPLE	ON	0 / 0 / 0 / 0	16:41:1
246	2581	S14mm-OPTOCBE	1	4	16:26:10	15:11 to 15:13	Aug 25, 2020	3C345	BACH/KISKY	81-20	POINT	OTF	ON	0 / 0 / 0 / 0	16:41:1
247	2581	S14mm-OPTOCBE	2	1	16:26:10	15:11 to 15:13	Aug 25, 2020	3C345	BACH/KISKY	81-20	POINT	OTF	ON	0 / 0 / 0 / 0	16:41:1
248	2581	S14mm-OPTOCBE	3	1	16:26:10	15:11 to 15:13	Aug 25, 2020	3C345	BACH/KISKY	81-20	POINT	OTF	ON	0 / 0 / 0 / 0	16:41:1
249	2581	S14mm-OPTOCBE	4	1	16:26:10	15:11 to 15:13	Aug 25, 2020	3C345	BACH/KISKY	81-20	POINT	OTF	ON	0 / 0 / 0 / 0	16:41:1

SQL state: active

Filters

Start time Aug/24/2020 15:44 Monday End time Aug/26/2020 15:44 Wednesday

Source Observer

Frontend Backend

Project ID Additional Filters

Display

SQL

Email/Save

```
# Create the subfolder for the frequency band to be analyzed
# and change into said directory.
> mkdir XX.XXGHz
> cd XX.XXGHz

# Create the scanlist, containing the scan numbers to be reduced,
# for the log-file and the used frequency (in MHz).
# This creates the "scanlist", the "scanlist.red" and
# "weather.dat", which provides weather information for each scan.
> dblog2scan_wea2.py ../obslog_202XXXXX.txt XXXXX

# Open "scanlist.red" and copy its content.
> cat scanlist.red

# Copy the analysis template into the working folder.
# Change X to
# 1.4cm for the 1.4cm receiver (19.25, 21.15, 22.85 and 24.75GHz)
# or to
# 7mm for the 7mm receiver (36.25, 28.75, 41.25 and 43.75GHz).
#
# This creates the directories
# "0.Raw", "1.Tsys+Poi", "2.Gain" and "3.Final",
# which will, step-by-step, be used for the analysis.
> cp -rf ~/cont_templates/X/* .

# Move into "0.Raw" and open the reducX.par file.
# For the 7mm receiver, it is called reduc7.par,
# while it is called reduc13.par for the 1.4cm receiver.
> cd 0.Raw/
> nedit reducX.par &
```

```

# Paste the content of the "scanlist.red"
# at the bottom of the newly opened window.
#
# Generally, there are two options on how to display the data:
# 1. use='(c[1]+c[2])/2'
# 2. use='(c[1]+c[2])/2-(c[3]+c[4])/2'
# Option 2 subtracts the data from the second horn,
# which observes an empty region near the source,
# from the signal itself.
# For good weather conditions option 1 should be used,
# while option 2 typically yields better results
# when the weather was not as good.
#
# In rare cases, a channel can malfunction, meaning it has to be
# excluded from above formulae.
#
# For data older than a month, the path to the data
# will be given by
# "fdir=/daten/mbfits/mbfits-202X-XX",
# where the X correspond to the month
# and the year of the observation.
#
# Make sure the "aver" option is turned on
# and that the data are plotted via "plot='/xs'".
#
# After doing all needed alterations,
# save the file before moving on.

# Execute the data reduction script.
# With the alterations mentioned above, the script will
# average over channel 1 and 2 and subtract
# the average of channel 3 and 4,
# and plot the scans in a PGPlot window.
#
# Here, a first quality check of the data can be conducted.
# The fits to the scans should be Gaussian, have their
# maximum near the center, where the offset is minimal,
# and have a positive amplitude.
#
# Pay attention to the HPBW (half-power beamwidth)
# of an observed calibrator or bright source
# and remember it for later.
> reduce2.py reducX.par

# Copy "flag.awk" into the working folder.
> cp ~/81-20/flag.awk .

# Alternatively to remembering the HPBW from the
# data reduction, it can also be checked by
# finding the scan number and used band of a calibrator
# via the obslog and the reducX.par file and plotting it.
> nedit ../../obslog_202XXXXX.txt &
> toolbox2 use='(c[1]+c[2])/2-(c[3]+c[4])/2' plot='/xs' useband=X fdir=/daten/mbfits/
  scan=XXXX aver

```

```

reduc13.par - /home/obs2/81-20/2020_08_25/19.25GHz/0.Raw/
File Edit Search Preferences Shell Macro Windows Help
scanlist scanlist.red weather.dat reduc13.par reduc13.par
# Parameter file to reduce 1.3cm SFK data
# with the toolbox
#
# Toolbox options start here
start_options
#
# Total power
# BB ch 1 and 2
# Horn 2 ch 3 and 4
#use='(c[1]+c[2])/2'
# Beam switch
use='(c[1]+c[2])/2-(c[3]+c[4])/2'
#
# Use XServer from PGPlot
plot='/xs'
#
# Make ps-or gif figure
#plot='/gif'
#plot
#
# Average scans in ALON and ALAT
aver
#
# RFI
#spikes=15
#
end_options
# End of Toolbox options
#
# Scan list starts here
#
# scan=0001
# scan=0002
# scan=0003
#
# Scan list starts here
# sub-scans can be deleted by the del= option
# in the second line: e.g.
# scan=0001
# del='1,4,5'
# to delete sub-scans 1, 4, and 5
#
# New root dir for data can be specified as e.g.
# fdir=/daten/mbfits/mbfits-2020-01
# default is /daten/mbfits
#
scan=2581 useband=4 fdir=/daten/mbfits/mbfits-2020-08/
scan=2583 useband=4 fdir=/daten/mbfits/mbfits-2020-08/
scan=2587 useband=4 fdir=/daten/mbfits/mbfits-2020-08/
scan=2588 useband=4 fdir=/daten/mbfits/mbfits-2020-08/
scan=2595 useband=4 fdir=/daten/mbfits/mbfits-2020-08/
scan=2596 useband=4 fdir=/daten/mbfits/mbfits-2020-08/
scan=2599 useband=4 fdir=/daten/mbfits/mbfits-2020-08/

```

```

# Execute the flag script, where X is an approximate
# HPBW value of a calibrator, and print the
# flagged scan numbers in a text-file.
# This script will flag all data that deviate too much
# from the given HPBW value, have a large offset from 0
# or have a negative amplitude and print out the reason
# for the flagging.
#
# Note: the error "awk: flag.awk:16: fatal: cannot open file 'X'
# for reading (No such file or directory)" is to be expected
# and does not hinder the script from working.
> awk -f flag.awk all.fit X > flag.txt
> nedit flag.txt &

```

```

# Inspect the flagged scans and try to improve the
# quality of the scan by bettering the reason why
# the scan got flagged.
#
# Omit "aver" to see each individual subscan,
# use "del=X" to delete certain subscons
# or "fcent=X" to define the center of the fit.
# Remove all subscons showing signs of radio frequency interference.
#
# Write all changes behind the corresponding scan
# in the reducX.par file.
# When no good fit is possible at all, comment the scan out
# by putting a "#" in front of it.
> toolbox2 use='(c[1]+c[2])/2-(c[3]+c[4])/2' plot='/xs' useband=X fdir=/daten/mbfits/
  scan=XXXX aver

# After working through the flag.txt file, save the changes
# and run the script again.
#
# This produces an "all.fit" file that contains all
# single fit-files, which will be used for all further programs.
> reduce2.py reducX.par

# Move to the next folder and copy the weather data here.
> cd ../1.Tsys+Poi/
> cp ../weather.dat .

# Grep ALON from the all.fit file and write all scan numbers
# with a result into the scanlist.
> grep ALON all.fit |awk '{print $2}' > scanlist

# The following step requires the input of the
# calibration temperature T_cal, which is different for
# each receiver and each frequency.
# They can be found at
  https://eff100mwiki.mpifr-bonn.mpg.de/doku.php?id=information\_for\_astronomers:rx\_list
# For the 7mm receiver, not all measured frequencies
# are given a T_cal in the wiki.
# Here, interpolating between the two nearest frequencies
# is a valid option.
# Although interpolation is reasonable, the accuracy of the
# final result will depend on the accuracy of the given T_cal.
#
# There are now two options on how to continue, where
# option 1 does not depend on the accuracy of T_cal
# as much as option 2 does.
# Additionally, option 2 only works when there are
# several scans covering a large range of elevations.

# Option 1 (Note: X is "1.3cm" for the 14mm receiver
# and "7mm" for the 7mm receiver):
> getwvr.py X

```

```

# Option 2:
# Here, X is the T_cal taken from the wiki.
# Executing the script prompts an input, which for this purpose is
# "Read weather.dat and create LIST.tsys" -> [l]
#
# "Opacities.eps" and "Weather.eps" provide additional information
# about the zenith opacity, the T_sys vs Air mass and
# other weather information.
> weather.py scanlist X
> gv Opacities.eps
> gv Weather.eps

# Execute the corr_point.py script with the same T_cal as above
# to apply the opacity corrections and correct the amplitudes
# for pointing offsets.
#
# This will prompt another input.
# If option 1 was used, the required input is
# "Apply data from Ef WVR (WVR.dat)" -> [w]
# If option 2 was used, the input is
# "Apply computed values (LIST.tsys)" -> [f]
> corr_point.py scanlist Tcal=X

# Move to the next folder, where the data will be
# corrected for gain elevation dependence and be
# converted from Kelvin to Jansky.
#
# Here, open and edit the "eff_flux.par" file.
> cd ../2.Gain/
> nedit eff_flux.par &

# Open the list of all observed sources, copy them and paste
# the list to the corresponding place in the eff_flux.par file.
# Change the number of sources in the square brackets accordingly.
#
# Note: the bracket needs to contain exactly 3 digits, so fill
# needed digits with blanks in front of the number
> LIST2sources.sh

```

```

eff_flux.par - /home/obs2/81-20/2020_08_25/19.25GHz/2.Gain/
File Edit Search Preferences Shell Macro Windows
##STEUERFILE FUER EFF_FLUX
ANZAHL QUELLEN: [ 17]
##Quellnamen: 8 Zeichen
0316+4119
1104+3811
1221+2813
1427+2348
1555+1111
1653+3945
1728+5013
1744+1935
1959+6508
2158-3013
2347+5142
3C286
3C295
3C345
BLLAC
MARS
NGC7027
##-----

```

```

# Open a list of known calibrators to find their flux densities.
# The inputs are the frequency (in GHz)
# and the epoch of the observation
# (the digit behind the "." indicates the fraction of the year
# that has already passed, meaning its value ranges from 0 to 9).
#
# Change the flux density of each observed calibrator
# in the eff_flux.par file, delete all the other ones
# and change the number of calibrators accordingly.
#
# Note: here the bracket has to have 2 digits,
# so again fill it with blanks.
> calibrators.py XX.XX 202X.X

```

```

ANZAHL KALIBRATORQUELLEN: [ 3]
##Angabe von Namen und Sollfluss in Jy ('3C286' 7.58)
'3C286'      2.79
'NGC7027'   5.74
'3C295'     1.15

```

```

# Change the gain corrections (Elevationskorrekturen) to the
# corresponding values found on the receiver page
# at the same link as above.

```

```

##-----
ANZAHL ELEVATIONSKORREKTUREN: [ 1]
##Quellnamen ('0836+71') oder 'allsour', Zeitintervall, Polynomkoeff. A0-A5
'allsour' 0.0 99999.9 0.954 3.19E-3 -5.42E-5 0.0 0.0 0.0
##-----

```

```

# Do the flux calibration.
#
# If this produces a "bad value during integer read" error,
# it is most probably due to an excess empty line
# or a wrong number of digits in one of the square brackets.
> eff_flux

# Check the calibration factor, transfer the value as well as
# its error to the eff_flux.par file and save it.
> cat Calibrators
##-----
ANZAHL KALIBRATIONEN: [ 1]
##Angabe mit Zeitintervall, Kal.-faktor,-fehler
0.0 99999.9 0.84139 0.08133
##-----

# Copy the content of the current working folder to
# 3.Final/ and move there.
#
# Note: the error
# "cp: cannot stat 'POL_raw': No such file or directory"
# is to be expected and does not affect the further analysis.
> cp * ../3.Final/
> cd ../3.Final/

# Execute eff_flux again to consider the calibration factor.
> eff_flux

# Done!
#
# To check if the calibration was done right,
# simply execute "cat Calibrators" again.
# The calibration factor should now be given as 1.0
# The final results are available via
> cat Averages

# More detailed information for each source can be accessed via
> cat FLUX.XXXX

# Repeat for every other frequency

# To get a better overview of all data and to get the correct
# flux density and error values, execute the "update_spectra.py"
# script in the main 81-20 folder.
> cd ../../..
> update_spectra.py

```

Listing B.1: Full guide on data reduction

```

# Create date-folder and all frequency folders in /home/obs2/81-20
# Open the Obslogger and export required data as a text file
> obslog

# Do the following for each frequency:

> dblog2scan_wea2.py ../obslog_202XXXXX.txt XXXXX

# Open "scanlist.red" and copy its content
> cat scanlist.red

> cp -rf ~/cont_templates/X/* .

> cd 0.Raw/
> nedit reducX.par &

# Paste the scanlist at the end of the file and
# change all options where necessary
> reduce2.py reducX.par

> cp ~/81-20/flag.awk .

# Here, X is the HPBW of a calibrator or bright source
> awk -f flag.awk all.fit X > flag.txt
> nedit flag.txt &

# Edit the "reducX.par" file with all needed
# alterations to the scans
> reduce2.py reducX.par

> cd ../1.Tsys+Poi/
> cp ../weather.dat .
> grep ALON all.fit |awk '{print $2}' > scanlist

# Use either option 1 or option 2.
# Option 1: X is "1.3cm" or "7mm"
> getwvr.py X

# Option 2: X is the T_Cal taken from the wiki.
# Use the "l" option.
> weather.py scanlist X

# Use either "w" or "f", depending on which option was used
> corr_point.py scanlist Tcal=X

> cd ../2.Gain/
> nedit eff_flux.par &

# Copy the source list and flux densities of the calibrators
# into the file, edit the number of sources/calibrators
# and the Elevationskorrekturen,
# and input the calibration factor and its error. Save the file.
> LIST2sources.sh
> calibrators.py XX.XX 202X.X
> eff_flux
> cat Calibrators

> cp * ../3.Final/
> cd ../3.Final/

> eff_flux

```

Listing B.2: Short guide for experienced people